

## Peierls instability due to the interaction of electrons with both acoustic and optical phonons in metallic carbon nanotubes

Marc Thilo Figge, Maxim Mostovoy, and Jasper Knoester

*Centre for Theoretical Physics and Materials Science Centre, University of Groningen, Nijenborgh 4, 9747 AG Groningen, The Netherlands*

(Received 17 July 2001; published 13 March 2002)

We consider Peierls instability due to the interaction of electrons with both acoustic and optical phonons in metallic carbon nanotubes, resulting in a static twist in the nanotube lattice below the critical temperature  $T_c$ . We study lattice excitations, the so-called solitwiston and polartwiston, over the ordered Peierls state for different types of boundary conditions. Furthermore, we calculate the electrical resistivity and find that our theory offers a possible explanation for the observed low-temperature rise in the electrical resistivity of carbon nanotubes.

DOI: 10.1103/PhysRevB.65.125416

PACS number(s): 63.20.Kr, 05.45.Yv, 63.70.+h, 72.80.Rj

### I. INTRODUCTION

It is well known that a half-filled conducting chain is unstable against a doubling of the unit cell, where the bond length between neighboring lattice sites alternates along the chain. The dimerization of the lattice results in an alternation of the electron hopping amplitudes leading to the opening of a Peierls gap in the electron spectrum and turning the system into a semiconductor. In this Peierls instability, the relevant phonons are the optical ones with wave vector  $q \sim 2k_F$ .<sup>1</sup> These phonons backscatter electrons from the left part of the Fermi surface with electron wave vector  $-k_F$  to the right one with electron wave vector  $+k_F$  and vice versa. It is usually assumed that above the phase-transition temperature  $T_c$  these phonons have a finite frequency  $\omega_o$  and we will, therefore, refer to them as optical phonons. Due to the mixing with the low-energy electron-hole excitations, these phonons soften and at  $T_c$  their frequency vanishes (giant Kohn anomaly).<sup>2</sup>

Recently, we have shown that *acoustic* phonons of small wave vector  $q$  and small frequency  $\omega_a(q) = v|q|$  may lead to a similar instability in metallic carbon nanotubes.<sup>3</sup> In fact, backscattering due to acoustic phonons always occurs if the size of the system's unit cell is the same above and below the transition temperature  $T_c$ . The reason is that in this case the phonon wave vector is only conserved up to a multiple of  $2k_F$ , such that optical- and acoustic-phonon modes of the same symmetry do exist which cooperate in the opening of the Peierls gap. As a specific example we considered the Peierls transition in metallic carbon nanotubes where, in the presence of both optical and acoustic phonons, the acoustic ones are the first to soften, which in this case means a vanishing of the phonon velocity at the Peierls transition temperature. A great deal of work has been done, e.g., to understand the role of electron-electron interactions in metallic carbon nanotubes which are typical candidates for an experimental realization of Luttinger liquid behavior. In this context the bosonization method has been applied,<sup>4,5</sup> as well as a mapping to a two-leg Hubbard model to describe the short-range Coulomb repulsion.<sup>6,7</sup> A different view is taken in our approach, where we, in fact, disregard electron correlations

and concentrate on the electron-lattice interaction which we assume to govern the system's low-temperature properties. The Peierls transition in metallic carbon nanotubes arising from the interaction with optical phonons has been studied before.<sup>8-12</sup> A general conclusion which has been drawn from these studies is that the opening of a Peierls gap is strongly suppressed for increasing nanotube diameters. This can be understood as the consequence of the fact that the elastic energy cost of the Peierls distortion grows proportional to the number of chains around the nanotube circumference. This conclusion remains valid when acoustic phonons are taken into account, however, the character of the Peierls distortion and topological excitation is new in this case, as we pointed out in Ref. 3.

In this paper, we give the detailed derivation of the model and its properties presented in Ref. 3. Moreover, we address the open question whether this model may offer a quantitative explanation for the observed low-temperature rise in the measured electrical resistivity of carbon nanotubes and, more generally, to what extent one may expect the Peierls transition and the associated softening of the acoustic phonons to be observable in such nanotubes. Finally, we show how the choice of boundary conditions imposed on the atomic lattice of a nanotube affects the properties in the low-temperature phase.

The outline of this paper is as follows: In Sec. II we start out by describing the nanotube lattice by the most general continuum model that is compatible with the symmetry of the hexagonal lattice. Next, we calculate the electron-lattice coupling for the long-wavelength phonon modes that result in the backscattering of electrons and develop an electron-lattice continuum model for armchair carbon nanotubes. Then, in Sec. III, we calculate the renormalized phonon frequencies at temperatures  $T > T_c$  and study the phase transition in the presence of both acoustic and optical phonons. Making use of the thus obtained renormalized acoustic-phonon frequency, we calculate in Sec. IV the temperature dependence of the electrical dc conductivity due to electron-phonon scattering. Topological excitations in the ordered Peierls phase ( $T < T_c$ ) are studied in Sec. V and we perform numerical simulations within an elastic spring model in Sec. VI for different types of boundary conditions on the atomic

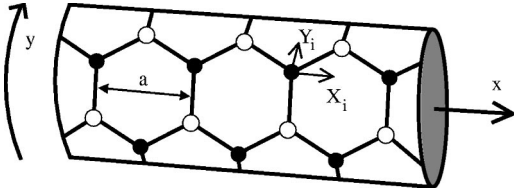


FIG. 1. Schematic picture of an armchair carbon nanotube. The open (○) and closed (●) circles denote the C ions of the two triangular sublattices  $i=A,B$ . The thick arrow points in the  $x$  direction along the nanotube axis and the definitions of the lattice displacements  $X_i, Y_i$  are indicated.

shifts. We discuss our results in Sec. VII and summarize and conclude this paper with Sec. VIII.

## II. DERIVATION OF THE ELECTRON-LATTICE CONTINUUM MODEL

Carbon nanotubes are well known for their unique electronic properties. Metallic carbon nanotubes can be subdivided in two classes:<sup>13</sup> (i) nominally metallic carbon nanotubes that are in fact semiconducting due to a curvature-induced energy gap proportional to the inverse square of their diameter, and (ii) metallic carbon nanotubes for which a curvature-induced energy gap does not exist by symmetry. The latter class is formed by the armchair carbon nanotubes to which we restrict our considerations in what follows. A so-called armchair carbon nanotube is shown in Fig. 1 and can be considered as composed of a finite number  $N_l$  of coupled two-leg ladders around its circumference. Each ladder consists of two coupled zigzag chains that are directed along the axis of the carbon nanotube. An effective low-energy model that describes the nanotube's electronic properties takes into account electrons that have zero momentum in the circumferential direction of the carbon nanotube and corresponds to a two-leg ladder tight-binding model.<sup>6,7</sup>

The corresponding electronic energy spectrum is shown in Fig. 2 for noninteracting electrons and is characterized by two Fermi points. At each Fermi point ( $n=1,2$ ) two electron bands that have a linear dispersion close to the Fermi energy,  $E=0$ , intersect. While the undistorted armchair carbon nanotube is a half-filled metallic system,<sup>14,15</sup> two types of electron backscattering (reverting the sign of the electron velocity) exist that can give rise to the opening of an energy gap in its electronic spectrum.

The dashed arrow in Fig. 2 indicates the usual backscattering, taking place between two different Fermi points. The relevant short-wavelength phonons correspond to the

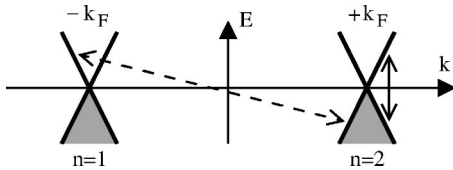


FIG. 2. Electron energy dispersion near the Fermi energy of a half-filled armchair carbon nanotube and the two types of backscattering processes distinguished in the text.

Kekulé structure of the carbon nanotube. In addition, however, a second type of backscattering exists, which is caused by long-wavelength phonons and leaves the electrons near the Fermi point (solid arrow). In what follows we will solely concentrate on the latter type of backscattering, which is responsible for the new type of Peierls distortion and topological excitation.<sup>3</sup>

To develop an electron-lattice continuum model for armchair carbon nanotubes we first derive a continuum model of the armchair carbon nanotube lattice. We consider the lattice of the armchair nanotube as an array of  $N$  connected rings at a distance  $a/2$  along the nanotube axis (see Fig. 1). Each ring contains  $2N_l$  carbon atoms, where  $N_l$  carbon atoms belong to each of the two triangular sublattices that build up the hexagonal nanotube lattice. We take into account lattice degrees of freedom in the cylindrical nanotube surface and, keeping in mind that the lattice distortion couples to electrons that have zero transverse momentum, we can disregard the dispersion of the atomic displacements in the circumferential direction. Thus, the time-dependent atomic displacement in the  $i$ th sublattice,

$$\vec{u}_i(x,t)=[X_i(x,t), Y_i(x,t)]^T, \quad (1)$$

is a function of the  $x$  coordinate along the nanotube axis only. Within the continuum model a ring of the nanotube lattice is characterized by the atomic displacements  $\vec{u}_i$  in the two sublattices  $i=A,B$  and by their spatial and time derivatives, respectively,  $\vec{u}'_i$  and  $\dot{\vec{u}}_i$ . It is convenient to introduce an eight-dimensional ring vector

$$\vec{R}(x,t)=(X_A, X'_A, Y_A, Y'_A, X_B, X'_B, Y_B, Y'_B)^T, \quad (2)$$

which combines all required information to describe the distortion in a ring along the nanotube axis.

The total lattice energy is the sum of the kinetic and the potential lattice energy  $H_{lat}=T+U$ . In terms of the ring vector  $\vec{R}$ , the kinetic lattice energy reads  $T=\frac{1}{2}\int dx \vec{R}^T \hat{\rho} \dot{\vec{R}}$ , where  $\hat{\rho}=(\rho_{lm})$  is the mass density matrix and  $l,m=1,\dots,8$ . The only nonzero elements  $\rho_{lm}$  are the diagonal elements that couple the time derivatives  $\dot{\vec{u}}_i$  of the atomic displacements. The potential energy in terms of the ring vector  $\vec{R}$  reads  $U=\frac{1}{2}\int dx \vec{R}^T \hat{K} \vec{R}$ , where the matrix  $\hat{K}=(k_{lm})$  couples all elements of  $\vec{R}$  in a ring ( $l,m=1,\dots,8$ ). We note that the matrix elements  $\rho_{lm}$  and  $k_{lm}$  are real and have to satisfy the conditions that the total lattice energy is invariant under (i) a constant shift of  $\vec{u}_A$  and  $\vec{u}_B$  that leaves the distance between the two sublattices unchanged, and (ii) a transformation  $\vec{R} \rightarrow \hat{U} \vec{R}$  that is allowed by the symmetry of the hexagonal nanotube lattice. As can be seen from Fig. 1, the hexagonal lattice is invariant under the reflection in the plane containing the carbon nanotube axis ( $\hat{P}_y$ ):  $y \rightarrow -y$ ,  $X_A \leftrightarrow X_B$ , and  $Y_A \leftrightarrow -Y_B$ , and in the plane perpendicular to the axis ( $\hat{P}_x$ ):  $x \rightarrow -x$ ,  $X_i \rightarrow -X_i$ , and  $Y_i \rightarrow Y_i$ . It then follows from the condition  $\hat{P} \hat{\rho} \hat{P}^T = \hat{\rho}$ , where  $\hat{P} = \hat{P}_x, \hat{P}_y$ , that the only nonzero elements  $\rho_{lm}$  are given by  $\rho_{11} = \rho_{55} = \rho_x$  and  $\rho_{33} = \rho_{77}$

$\equiv \rho_y$ . Furthermore, the condition  $\hat{P}\hat{K}\hat{P}^T = \hat{K}$ , where again  $\hat{P} = \hat{P}_x, \hat{P}_y$ , together with condition (i) given above, reduce the number of free coupling parameters  $k_{lm}$  from 36 to a set of eight parameters. It is convenient to define four new functions  $X_{\pm}, Y_{\pm}$  by the symmetric and antisymmetric combinations  $X_{\pm} = (X_A \pm X_B)/\sqrt{2}$  and  $Y_{\pm} = (Y_A \pm Y_B)/\sqrt{2}$ . The total lattice energy is then given by the expression

$$H_{lat} = \frac{1}{2} \int dx [\rho_x (\dot{X}_+^2 + \dot{X}_-^2) + \rho_y (\dot{Y}_+^2 + \dot{Y}_-^2) + \alpha_x X_-^2 + \alpha_y Y_-^2 + \beta_x X_+'^2 + \beta_y Y_+'^2 + \gamma_x X_-'^2 + \gamma_y Y_-'^2 + 2\delta_x X_- Y_+' + 2\delta_y Y_- X_+'], \quad (3)$$

which represents the most general continuum model of the armchair carbon nanotube lattice compatible with its symmetry and is determined by the set  $\{\alpha_x, \alpha_y, \beta_x, \beta_y, \gamma_x, \gamma_y, \delta_x, \delta_y\}$  of coupling parameters.

We can write Eq. (3) in a more compact form, if we define a new ring vector  $\vec{\mathcal{R}} = (X_+, Y_+, X_-, Y_-)^T$ , and use the ansatz  $\vec{\mathcal{R}}(x, t) = 1/\sqrt{N} \sum_q \vec{\mathcal{R}}_q \exp(iqx - i\omega t)$ . The total lattice energy is then obtained in the simple form  $H_{lat} = \frac{1}{2} \sum_q \vec{\mathcal{R}}_q^\dagger \hat{h}_{lat} \vec{\mathcal{R}}_q$ , where the matrix  $\hat{h}_{lat}$  reads

$$\hat{h}_{lat} = \frac{a}{2} \begin{pmatrix} \omega^2 \rho_x & 0 & 0 & iq\delta_y \\ +q^2 \beta_x & & & \\ 0 & \omega^2 \rho_y & -iq\delta_x & 0 \\ & +q^2 \beta_y & & \\ 0 & iq\delta_x & \omega^2 \rho_x + \alpha_x & 0 \\ & & +q^2 \gamma_x & \\ -iq\delta_y & 0 & 0 & \omega^2 \rho_y + \alpha_y \\ & & & +q^2 \gamma_y \end{pmatrix}. \quad (4)$$

It is easy to check that  $\hat{h}_{lat}$  is invariant under the parity transformation

$$\hat{p} = \begin{pmatrix} 1 & 0 & 0 & 0 \\ 0 & -1 & 0 & 0 \\ 0 & 0 & -1 & 0 \\ 0 & 0 & 0 & 1 \end{pmatrix} \quad \text{with } \hat{p}^2 = I, \quad (5)$$

where  $I$  is the unit matrix. It thus follows that the four eigenmodes of the lattice Hamiltonian  $H_{lat}$  can be classified by their parity  $\hat{p}\vec{\mathcal{R}}_{\pm} = \pm\vec{\mathcal{R}}_{\pm}$ , where  $\vec{\mathcal{R}}_- = (0, Y_+, X_-, 0)^T$  and  $\vec{\mathcal{R}}_+ = (X_+, 0, 0, Y_-)^T$ . The negative-parity mode describes a bond-length alternation along the nanotube axis ( $X_A = -X_B$  and  $Y_A = Y_B$ ), which is out of phase in neighboring zigzag chains of the armchair nanotube lattice. The two eigenmodes that belong to the negative-parity mode  $\vec{\mathcal{R}}_-$  are (i) an optical-phonon mode with amplitude  $u_o(x, t)$  and frequency  $\omega_o$ ,

$$\frac{\partial^2}{\partial t^2} u_o(x, t) = -\omega_o^2 u_o(x, t), \quad \omega_o \approx \sqrt{\frac{\alpha_x}{\rho_x}}, \quad (6)$$

and (ii) an acoustic-phonon mode with amplitude  $u_a(x, t)$ ,

$$\frac{\partial^2}{\partial t^2} u_a(x, t) = v_0^2 \frac{\partial^2}{\partial x^2} u_a(x, t), \quad (7)$$

frequency  $\omega_a(q) \approx v_0 |q|$ , and phonon velocity

$$v_0 = \left( \frac{\beta_y}{\rho_y} - \frac{\delta_x^2}{\rho_x \alpha_x} \right)^{1/2}. \quad (8)$$

On the other hand, the positive-parity mode describes a shift of the two sublattices against each other in the circumferential direction ( $Y_A = -Y_B$  and  $X_A = X_B$ ). This does not affect the length of the bonds along the nanotube axis. To the positive-parity mode  $\vec{\mathcal{R}}_+$  belongs an optical-phonon mode with frequency  $\bar{\omega}_o \approx \sqrt{\alpha_y/\rho_y}$ , and an acoustic-phonon mode  $\bar{\omega}_a(q)$  with phonon velocity  $\bar{v}_0 = [\beta_x/\rho_x - \delta_y^2/(\rho_x \alpha_y)]^{1/2}$ . In what follows we will show explicitly that the optical- and acoustic-phonon modes which belong to the negative-parity mode, respectively, Eqs. (6) and (7), will cause the back-scattering of electrons for small  $q$ .

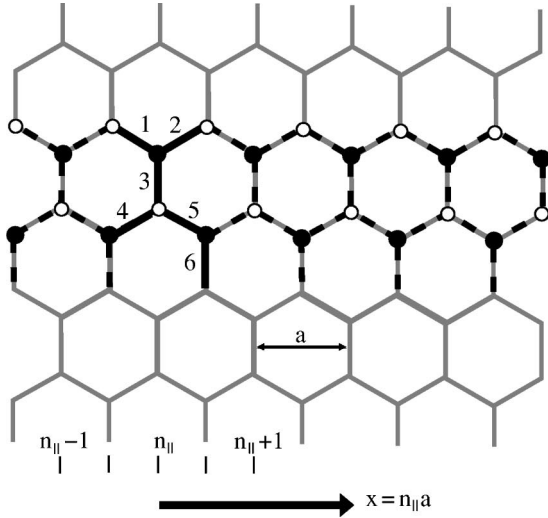
The effective low-energy model describing free electrons in the armchair carbon nanotube corresponds to a two-leg ladder tight-binding model.<sup>6,7</sup> At all relevant temperatures, the electrons have zero transverse momentum around the circumference of the carbon nanotube and can only propagate in the  $x$  direction along its axis. Here, we generalize the Hamiltonian of the two-leg ladder model and take into account that the electron hopping amplitudes depend on the interatomic distances between the electronic orbitals on neighboring atoms. Figure 3 visualizes the notation that is used to write the two-leg ladder Hamiltonian in the compact form

$$H_{arm} = - \sum_{n_{\parallel}, \sigma} \sum_{j=1}^6 T_j (d_{A\sigma}^\dagger(n_{\parallel}a + a_j) d_{B\sigma}(n_{\parallel}a + b_j) + \text{H.c.}). \quad (9)$$

The fermionic operator  $d_{i\sigma}(n_{\parallel}a)$  [ $d_{i\sigma}^\dagger(n_{\parallel}a)$ ] annihilates (creates) an electron in sublattices  $i=A, B$  with spin  $\sigma$  at position  $x = n_{\parallel}a$  along the nanotube axis. The electron hopping amplitudes depend on the atomic displacements, Eq. (1), and take the form

$$T_j = t_j + \frac{\alpha_j}{\sqrt{N_l}} \vec{e}_j \cdot [\vec{u}_B(n_{\parallel}a + b_j) - \vec{u}_A(n_{\parallel}a + a_j)]. \quad (10)$$

Here,  $t_j$  denotes the hopping amplitude in the absence of electron-lattice interactions, while  $\alpha_j/\sqrt{N_l}$  is the electron-lattice coupling and  $\vec{e}_j$  is a unit vector which is oriented along bond  $j$ . The explicit expressions of the electron hopping amplitudes  $T_j$  are summarized in the table of Fig. 3 and satisfy the condition that  $H_{arm}$  has to be invariant under the reflection symmetry  $\hat{P}_y$ .



j	$t_j$	$\alpha_j$	$\vec{e}_j$	$a_j$	$b_j$
1	$t_{  }$	$\alpha_{  }$	$\vec{e}_1$	0	$-a/2$
2	$t_{  }$	$\alpha_{  }$	$\vec{e}_2$	0	$a/2$
3	$t_{\perp}$	$\alpha_{\perp}$	$\vec{e}_3$	0	0
4	$t_{  }$	$\alpha_{  }$	$\vec{e}_4$	$-a/2$	0
5	$t_{  }$	$\alpha_{  }$	$\vec{e}_5$	$a/2$	0
6	$t_{\perp}$	$\alpha_{\perp}$	$\vec{e}_6$	$a/2$	$a/2$

$$\begin{aligned} \vec{e}_1 &= (-\sqrt{3}/2, 1/2) \\ \vec{e}_2 &= (+\sqrt{3}/2, 1/2) \\ \vec{e}_3 &= (0, -1) \\ \vec{e}_4 &= -\alpha_3 \vec{e}_1 \\ \vec{e}_5 &= -\alpha_3 \vec{e}_2 \\ \vec{e}_6 &= -\alpha_3 \vec{e}_3 \end{aligned}$$

FIG. 3. The unrolled armchair carbon nanotube lattice corresponds to a graphene sheet (solid grey lines) which is composed of a ladder repeat unit around the nanotube circumference as indicated by the dashed black lines. The repeat unit of such a ladder in the direction of the nanotube axis is drawn with solid black lines. The two triangular sublattices  $i=A,B$  are depicted by, respectively, ‘‘●’’ and ‘‘○’’, and the hopping amplitudes  $T_j$  are obtained from the table in combination with Eq. (10).

We now derive the continuum version of the Hamiltonian  $H_{arm}$  which will model the system close to the Fermi points. This is done by interpreting  $x$  as a continuous variable in the direction of the nanotube axis and by representing the operator  $d_{i\sigma}(x)$  close to each Fermi point as a product of two factors,

$$d_{i\sigma}(x) \approx \sqrt{\frac{a}{2}} (e^{ik_F x} \psi_{i,1,\sigma}(x) + e^{-ik_F x} \psi_{i,2,\sigma}(x)). \quad (11)$$

The exponential factor varies fast along the nanotube axis on the scale of the lattice constant  $a \sim k_F^{-1}$ , while the second factor is the slowly varying function  $\psi_{i,n,\sigma}$  at Fermi points  $n=1,2$  and is related to the small deviation of the electron momentum from the Fermi wave vector  $\pm k_F$ . In the absence of the electron-lattice coupling  $\alpha_j=0$ , we obtain from Eq. (9) the kinetic energy of the electrons,

$$H_{el} = \frac{v_F}{i} \sum_{n,\sigma} \int dx \Psi_{n,\sigma}^\dagger(x) \sigma_3 \frac{\partial}{\partial x} \Psi_{n,\sigma}(x), \quad (12)$$

where  $\sigma_3$  is the Pauli matrix. The spinor  $\Psi_{n,\sigma}(x) \equiv [\psi_{R,n,\sigma}(x), \psi_{L,n,\sigma}(x)]^T$  is given by

$$\Psi_{n,\sigma}(x) = \frac{1}{\sqrt{2}} \begin{pmatrix} 1 & (-1)^n \\ i & -i(-1)^n \end{pmatrix} \begin{pmatrix} \psi_{A,n,\sigma}(x) \\ \psi_{B,n,\sigma}(x) \end{pmatrix} \quad (13)$$

in terms of the slowly varying functions  $\psi_{i,n,\sigma}$ . It describes left-moving  $[\psi_{L,n,\sigma}(x)]$  and right-moving  $[\psi_{R,n,\sigma}(x)]$  electrons at the two Fermi points  $n=1,2$  with Fermi velocity  $v_F = at_{||} \sin(k_F a/2)$  and Fermi wave vector  $k_F = (2/a) \arccos[-t_{\perp}/(2t_{||})]$ . Thus,  $H_{el}$  describes the kinetic energy of electrons in two electron bands that intersect with linear dispersion at each of the two Fermi points (see Fig. 2).

For a finite coupling  $\alpha_j$ , we obtain from Eq. (9) the electron-lattice Hamiltonian

$$\begin{aligned} H_{el-lat} &= \sum_{n,\sigma} \int dx \Psi_{n,\sigma}^\dagger(x) \sigma_1 \Psi_{n,\sigma}(x) \\ &\quad \times \sum_j (T_j - t_j) \frac{\sin[k_F(a_j - b_j)]}{2}, \end{aligned} \quad (14)$$

which contains the Pauli matrix  $\sigma_1$  and describes the backscattering of electrons at each Fermi point  $n$ . In the derivation of this expression, forward-scattering contributions have been omitted, as these processes are of the type  $\Psi_{n,\sigma}^\dagger(x) \Psi_{n,\sigma}(x)$  and do not lead to an instability. After performing the sum over  $j$  we find

$$\begin{aligned} H_{el-lat} &= \sqrt{6} \frac{\alpha_{||}}{\sqrt{N_l}} \sin\left(k_F \frac{a}{2}\right) \sum_{n,\sigma} \int dx \Psi_{n,\sigma}^\dagger(x) \sigma_1 \Psi_{n,\sigma}(x) \\ &\quad \times \left[ X_- - \frac{a}{4\sqrt{3}} \frac{\partial Y_+}{\partial x} \right], \end{aligned} \quad (15)$$

which shows that, as expected, the backscattering of electrons only depends on  $X_-$  and  $Y_+$ . The latter are linear combinations of the optical- and acoustic-phonon modes defined in Eqs. (6) and (7), respectively. The shifts  $X_-$  and  $Y_+$  and the amplitudes  $u_o$  and  $u_a$  are related by

$$X_- = \frac{\delta_x}{\alpha_x} \frac{\partial}{\partial x} u_a + u_o; \quad Y_+ = -u_a - \frac{\delta_x}{\alpha_x} \frac{\rho_x}{\rho_y} \frac{\partial}{\partial x} u_o \quad (16)$$

or

$$u_o = X_- + \frac{\delta_x}{\alpha_x} \frac{\partial}{\partial x} Y_+; \quad u_a = -Y_+ - \frac{\delta_x}{\alpha_x} \frac{\rho_x}{\rho_y} \frac{\partial}{\partial x} X_- \quad (17)$$

We thus see that the optical- as well as the acoustic-phonon modes involve atomic shifts in both the directions perpendicular and parallel to the nanotube's axis. However, within a somewhat simplified picture restricted to lowest order in the derivatives, the optical phonons correspond to a relative shift of the nanotube's two triangular sublattices against each other along its axis:  $u_o \sim (X_A - X_B)/\sqrt{2}$ . This then leads to a

lattice deformation with out-of-phase bond-length dimerization in neighboring zigzag chains along the nanotube axis. Similarly, the acoustic phonons which describe a twist distortion of the cylindrical nanotube lattice  $u_a \sim (Y_A + Y_B)/\sqrt{2}$  also result in an out-of-phase bond-length dimerization. The electron-lattice interaction Eq. (15) is finally written in the convenient form

$$H_{el-lat}[\Delta_o + \Delta_a] = \sum_{n,\sigma} \int dx \Psi_{n,\sigma}^\dagger(x) (\Delta_o + \Delta_a) \sigma_1 \Psi_{n,\sigma}(x). \quad (18)$$

Here, we introduced the ‘‘order parameter’’  $\Delta_i$  for optical ( $i=o$ ) and acoustic ( $i=a$ ) phonons, which to the lowest order in the derivatives of the phonon amplitude  $u_i$  are given by

$$\begin{aligned} \Delta_o &= \sqrt{6} \frac{\alpha_{\parallel}}{\sqrt{N_l}} \sin\left(k_F \frac{a}{2}\right) u_o, \\ \Delta_a &= \sqrt{6} \frac{\alpha_{\parallel}}{\sqrt{N_l}} \sin\left(k_F \frac{a}{2}\right) \left[ \frac{\delta_x}{\alpha_x} + \frac{1}{4} \frac{a}{\sqrt{3}} \right] \frac{\partial}{\partial x} u_a. \end{aligned} \quad (19)$$

As is clear from Eq. (18), the difference between the optical and acoustic phonons is that  $\Delta_o$  is proportional to the amplitude  $u_o$ , while  $\Delta_a$  is proportional to the derivative of the amplitude  $\partial u_a / \partial x$ . Since in the ordered state this implies that  $X_-$  is of the same order as  $aY_+$ , one may doubt the validity of the continuum approximation used above. Therefore, we performed numerical calculations of the optimal lattice configuration at  $T=0$ , which are presented in Sec. VI, and prove this approach to be valid.

To summarize, we study the Peierls transition due to both optical and acoustic phonons starting from the continuum electron-lattice Hamiltonian

$$H = H_{el} + H_{el-lat}[\Delta_o + \Delta_a] + H_{lat}[\Delta_o] + H_{lat}[\Delta_a], \quad (20)$$

where  $H_{el}$  and  $H_{el-lat}$  are given by, respectively, Eq. (12) and Eq. (18). The last two terms in Eq. (20) represent the lattice energy of the relevant optical ( $i=o$ ) and acoustic ( $i=a$ ) phonons,

$$H_{lat}[\Delta_i] = \frac{N_F}{\pi \lambda_i v_F} \int dx \Delta_i^2 + \frac{1}{2\rho_i} \int dx \pi_i^2, \quad (21)$$

where the momentum density is given by  $\pi_i(x,t) = \rho_i \partial u_i(x,t) / \partial t$  and contains the corresponding mass densities ( $\rho_o = \rho_x$  and  $\rho_a = \rho_y$ ). We introduced in Eq. (21) the factor  $N_F$  which denotes the number of Fermi points,  $n = 1, \dots, N_F$ , at which two-electron bands cross with linear energy dispersion. The dimensionless electron-lattice coupling constant for the optical ( $i=o$ ) and acoustic ( $i=a$ ) phonon modes is defined by

$$\lambda_i \equiv \frac{2N_F}{\pi v_F} \frac{2|g_i|^2}{\omega_i} \quad (22)$$

and absorbs a factor  $N_F$ , while  $g_i$  is the electron-lattice coupling constant defined below by Eq. (24). For  $\Delta_a=0$  and

$N_F=1$  the Hamiltonian Eq. (20) coincides with the Hamiltonian of the Takayama-Lin-Liu-Maki (TLM) model. This is the continuum version of the Su-Schrieffer-Heeger model for *transpolyacetylene*.<sup>16,17</sup> On the other hand, for  $\Delta_o=0$  and  $N_F=2$ , the Hamiltonian Eq. (20) is equivalent to the Hamiltonian describing the electron-twistion interactions in the armchair carbon nanotubes.<sup>13,18</sup> An order parameter  $\Delta_a = \text{const}$  corresponds to a uniform twist deformation of the armchair carbon nanotube; such a twist was, in fact, recently observed using scanning tunneling microscopy.<sup>19</sup>

### III. PEIERLS TRANSITION WITH ACOUSTIC AND OPTICAL PHONONS

We consider the Peierls transition in the electron-lattice system Eq. (20). The coupling of the phonons to electrons has two effects which have to be taken into account in a self-consistent treatment of the system dynamics: (i) a renormalization of the optical- and acoustic-phonon frequencies, and (ii) a mixing of the two phonon modes due to electron-hole excitations. Applying a Fourier transformation, the Hamiltonian Eq. (20) in momentum space is given by

$$\begin{aligned} H &= \sum_{n,\sigma} \sum_{s=\pm} \sum_p \left[ \varepsilon_n^s(p) c_{n,s,\sigma}^\dagger(p) c_{n,s,\sigma}(p) \right. \\ &+ \sum_{i=a,o} \sum_q \frac{sg_i(q)}{\sqrt{L}} (b_i(q) + b_i^\dagger(-q)) c_{n,s,\sigma}^\dagger(p) \\ &\left. \times c_{n,-s,\sigma}(p-q) \right] + \sum_{i=a,o} \sum_q \omega_i(q) \left( b_i^\dagger(q) b_i(q) + \frac{1}{2} \right). \end{aligned} \quad (23)$$

Here, the fermionic operator  $c_{n,s,\sigma}^\dagger(p)$  [ $c_{n,s,\sigma}(p)$ ] denotes the creation (annihilation) of an electron with spin projection  $\sigma$  and small momentum  $|p| \ll k_F$  measured from the Fermi point  $n$ . The index  $s$  refers to right- ( $s=+$ ) and left- ( $s=-$ ) moving electrons with linear energy dispersion  $\varepsilon_n^s(p) = sv_F p$ . The second term in the Hamiltonian is obtained from the quantization of the atomic displacements and describes the backscattering of the electrons ( $s=\pm \leftrightarrow s=\mp$ ) due to the interaction with acoustic and optical phonons. The creation (annihilation) of an acoustic ( $i=a$ ) or optical ( $i=o$ ) phonon with small momentum  $q$  is represented by the bosonic operator  $b_i^\dagger(q)$  [ $b_i(q)$ ] and the corresponding electron-lattice coupling constants  $g_i(q)$  are given by

$$\begin{aligned} g_o &= \sqrt{6} \frac{\alpha_{\parallel}}{\sqrt{N_l}} \sin\left(k_F \frac{a}{2}\right) \frac{i}{\sqrt{2\rho_o \omega_o}}, \\ g_a &= \sqrt{6} \frac{\alpha_{\parallel}}{\sqrt{N_l}} \sin\left(k_F \frac{a}{2}\right) \left[ \frac{\delta_x}{\alpha_x} + \frac{1}{4} \frac{a}{\sqrt{3}} \right] \frac{-q}{\sqrt{2\rho_a \omega_a(q)}}. \end{aligned} \quad (24)$$

It thus follows that the coupling  $g_a(q)$  to the acoustic phonon with frequency  $\omega_a = v_o |q|$  is proportional to  $\sqrt{q}$ , whereas the coupling to the optical phonon  $g_o(q)$  is approximately constant with finite frequency  $\omega_o$ . We note that,

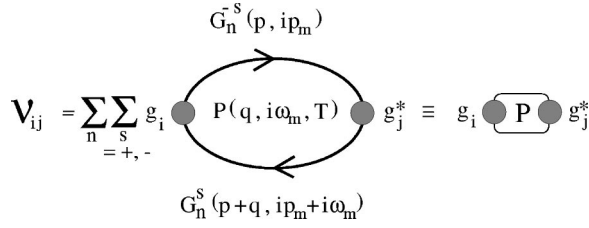


FIG. 4. Feynman diagram of the matrix element  $\mathcal{V}_{ij}$  of the interaction matrix Eq. (26).

though the coupling to acoustic phonons  $g_a(q)$  is small for small  $q$ , the actual strength of the interaction is given by the dimensionless electron-lattice coupling Eq. (22) which is finite both for optical and acoustic phonons. The lattice energy of the two modes is given by the third term in Eq. (23).

Let us consider the temperature dependence of the optical- and acoustic-phonon frequencies at temperatures  $T$  above the critical temperature  $T_c$ . The bare phonon propagator  $\mathcal{D}_0$  is formally written in terms of a  $2 \times 2$  matrix,

$$\mathcal{D}_0 = \begin{pmatrix} D_a^0 & 0 \\ 0 & D_o^0 \end{pmatrix}. \quad (25)$$

This matrix contains the bare acoustic- ( $i=a$ ) and optical- ( $i=o$ ) phonon propagator  $D_i^0(\omega_i, i\omega_m) = -2\omega_i / (\omega_m^2 + \omega_i^2)$  with the bosonic Matsubara frequency  $\omega_m = 2m\pi T$  ( $m$  is an integer number) and the bare phonon frequency  $\omega_i$ . Similarly, the free particle Green's function is defined by  $G_n^s(p, ip_m) = 1/[ip_m - \varepsilon_n^s(p)]$ , with the fermionic Matsubara frequency  $p_m = (2m+1)\pi T$  ( $m$  is an integer number). In the matrix formalism, the coupling of the phonons to electrons is given by the interaction matrix

$$\mathcal{V} = \begin{pmatrix} g_a g_a^* & g_a g_o^* \\ g_o g_a^* & g_o g_o^* \end{pmatrix} P(q, i\omega_m, T), \quad (26)$$

which contains the vacuum polarization  $P(q, i\omega_m, T)$ . The Feynman diagram of an interaction matrix element  $\mathcal{V}_{ij}$  is shown in Fig. 4. The vacuum polarization describes an electron-hole excitation and recombination by absorption and emission of a phonon with momentum  $q$  and (Matsubara) frequency  $i\omega_m$ . In terms of the particle Green's function  $G_n^s(p, ip_m)$  the vacuum polarization reads

$$P(q, i\omega_m, T) = \sum_n \frac{2}{L} \sum_p T \sum_{ip_m} \{ G_n^+(p, ip_m) G_n^-(p+q, ip_m + i\omega_m) + G_n^-(p, ip_m) G_n^+(p+q, ip_m + i\omega_m) \}. \quad (27)$$

The summation is over the internal variables at each Fermi point  $n$  with  $p$  the particle momentum and  $ip_m$  the particle energy, while the factor 2 accounts for the spin degrees of freedom. An elegant way to calculate  $P(q, \omega, T) = \text{Re}[P] + i \text{Im}[P]$  is presented in Ref. 20, where we obtain the analytical expressions

$$\begin{aligned} \text{Re}[P] = & -\frac{2N_F}{\pi v_F} \left\{ \ln \frac{\gamma W}{\pi T} - \frac{1}{4} \left[ \Psi \left( \frac{1}{2} - i \frac{v_F q + \omega}{4\pi T} \right) \right. \right. \\ & + \Psi \left( \frac{1}{2} + i \frac{v_F q - \omega}{4\pi T} \right) + \Psi \left( \frac{1}{2} - i \frac{v_F q - \omega}{4\pi T} \right) \\ & \left. \left. + \Psi \left( \frac{1}{2} + i \frac{v_F q + \omega}{4\pi T} \right) - 4 \Psi \left( \frac{1}{2} \right) \right] \right\} \quad (28) \end{aligned}$$

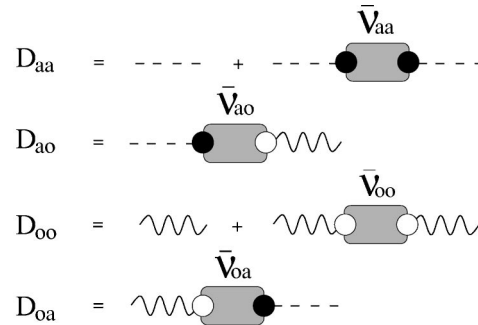
for the real part and

$$\text{Im}[P] = -\frac{N_F}{v_F} \frac{\sinh \left( \left| \frac{\omega}{2T} \right| \right)}{\cosh \left( \frac{\omega}{2T} \right) + \cosh \left( \frac{v_F q}{2T} \right)} \quad (29)$$

for the imaginary part. Here,  $\Psi(z) = (d/dz) \ln \Gamma(z)$  is the digamma function,  $W$  is the energy cutoff which is of the order of the electron bandwidth ( $\sim 10$  eV), and  $\gamma = 1.781072 \dots$  denotes the exponential of Euler's constant.

We proceed with the calculation of the renormalized acoustic- and optical-phonon frequencies using the random-phase approximation. The propagation of phonons that are dressed by the interaction with the electrons is described by the matrix

$$\mathcal{D} = \begin{pmatrix} D_{aa} & D_{ao} \\ D_{oa} & D_{oo} \end{pmatrix}, \quad (30)$$



with

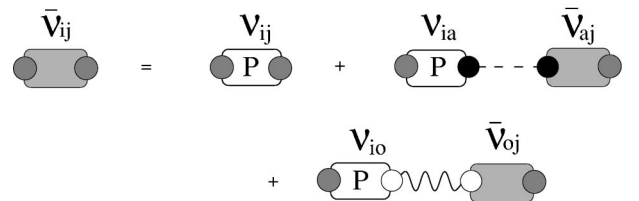


FIG. 5. Feynman diagrams of the matrix elements  $D_{i,j}$  of the dressed phonon propagation matrix Eq. (30). The bare acoustic- (optical-) phonon propagator  $D_a^0$  ( $D_o^0$ ) is represented by a dashed (wiggled) line and the corresponding coupling  $g_a$  ( $g_o$ ) by “●” (“○”). The diagrammatic symbol for the element  $\mathcal{V}_{ij}$  of the interaction matrix was introduced in Fig. 4 and is the building block in the Dyson equation for the dressed element  $\bar{\mathcal{V}}_{ij}$ , which contains electron-hole excitations that are coupled by all possible combinations of acoustic- and optical-phonon lines.

which is related to the bare phonon propagation matrix  $\mathcal{D}_0$  by  $\mathcal{D} = \mathcal{D}_0 + \mathcal{D}_0 \bar{\mathcal{V}} \mathcal{D}_0$ . In other words,  $\mathcal{D}$  differs from  $\mathcal{D}_0$  by the interaction between the electrons and phonons denoted by  $\bar{\mathcal{V}}$ . Within the random-phase approximation this interaction matrix is the solution of the Dyson equation  $\bar{\mathcal{V}} = \mathcal{V} + \mathcal{V} \mathcal{D}_0 \bar{\mathcal{V}}$ , which describes the renormalization of the bare interaction matrix Eq. (26) due to the internal coupling of electron-hole excitations by the acoustic and optical phonons. The Feynman diagrams of the processes that are included in the calculation of the dressed phonon propagation matrix are shown in Fig. 5. The renormalized optical- and acoustic-phonon frequencies denoted by  $\tilde{\omega}_o(q)$  and  $\tilde{\omega}_a(q)$ , respectively, are found from the poles of  $\det(\mathcal{D})$ , or, equivalently, by solving  $\det(\mathcal{D}_0^{-1} - \mathcal{V}) = 0$ . This condition can be rewritten in the form  $(\omega_m \rightarrow -i\omega)$

$$\omega^4 - \omega^2(\omega_a^2 f_a + \omega_o^2 f_o) + \omega_a^2 \omega_o^2 (f_a + f_o - 1) = 0, \quad (31)$$

where the vacuum polarization is hidden in

$$f_i \equiv 1 + \lambda_i \frac{\pi v_F}{2N_F} P(q, \omega, T), \quad (32)$$

and  $\lambda_i$  is the dimensionless electron-lattice coupling of the optical- ( $i=o$ ) and acoustic- ( $i=a$ ) phonon modes as defined by Eq. (22). We plot in Fig. 6 the numerically obtained solutions of Eq. (31) for various different temperatures  $T \geq T_c$ . We take the full  $\omega$  and  $q$  dependencies of  $P(q, \omega, T)$  into account in these calculations. Furthermore, we set  $\lambda_a = \lambda_o = 0.05$ , the Fermi velocity  $v_F = 5.3 \text{ eV \AA}$ , the bandwidth  $W = 10 \text{ eV}$ , while the frequency of the bare optical-phonon mode  $\omega_o = 0.18 \text{ eV}$ , and the bare acoustic-phonon velocity  $v_o = 0.09 \text{ eV \AA}$ . As can be seen in Fig. 6, the optical-phonon frequency is found to be shifted towards lower frequencies but does not change qualitatively as a function of  $q$ . In contrast, the acoustic-phonon velocity is seen to change qualitatively relative to the phonon velocity of the bare acoustic mode and to vanish for small phonon momentum  $q$  at the transition temperature  $T = T_c$ .

Analytical expressions for the renormalized phonon frequencies are obtained in the limits  $\tilde{\omega}_a(q) \ll T$  and  $\tilde{\omega}_a(q) \ll \tilde{\omega}_o(q)$ , where the static expression of the vacuum polarization for phonon momenta  $v_F q \ll T$  can be used,

$$P(q, 0, T) \approx -\frac{2N_F}{\pi v_F} \left\{ \ln \frac{\gamma W}{\pi T} - c \left( \frac{v_F q}{T} \right)^2 \right\}, \quad (33)$$

with the constant  $c = 7\zeta(3)/(16\pi^2)$  containing Riemann's zeta function. In this limit we obtain from Eq. (31) the solution

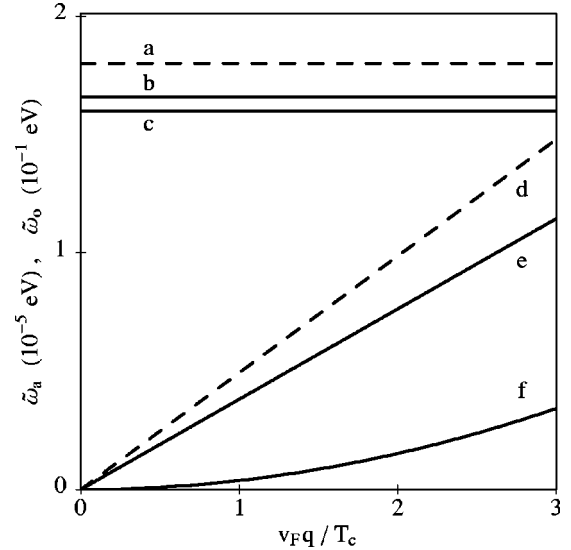


FIG. 6. Numerical results for the renormalized phonon frequencies  $\tilde{\omega}_a(q)$  and  $\tilde{\omega}_o$  as a function of the phonon momentum  $q$ . We set  $\lambda_a = \lambda_o = 0.05$  and plot the dispersions for various values of the temperature  $T$ . (a) The bare optical-phonon frequency (dashed) is shifted towards lower frequencies (b) at  $T = 1000T_c$  and (c) at  $T = T_c$ . (d) The bare phonon velocity of the acoustic mode (dashed) is decreased (e) at  $T = 100T_c$  and (f) at  $T = T_c$  even vanishes in the limit  $q \rightarrow 0$ .

$$\tilde{\omega}_a^2(q) = \omega_a^2(q) \left[ \frac{1 - (\lambda_o + \lambda_a) \ln \frac{\gamma W}{\pi T}}{1 - \lambda_o \ln \frac{\gamma W}{\pi T}} + c \lambda_a \left( \frac{v_F q}{T \left( 1 - \lambda_o \ln \frac{\gamma W}{\pi T} \right)} \right)^2 \right] \quad (34)$$

for the acoustic-phonon mode. The optical-phonon frequency is hardly affected if  $\tilde{\omega}_o(q) \gg T$  as is the case for the parameters in the simulation that yielded Fig. 6, while in the opposite limit [ $\tilde{\omega}_o(q) \ll T$ ] it becomes

$$\tilde{\omega}_o^2(q) = \omega_o^2 \left( 1 - \lambda_o \left\{ \ln \frac{\gamma W}{\pi T} - c \left( \frac{v_F q}{T} \right)^2 \right\} \right). \quad (35)$$

We thus see that the expression for the renormalized optical frequency is independent of  $\lambda_a$  and is the same as in the absence of the coupling to acoustic phonons. On the other hand, the renormalized acoustic-phonon frequency depends on the sum

$$\lambda \equiv \lambda_a + \lambda_o. \quad (36)$$

As a result, the acoustic phonons soften first at the critical temperature given by

$$T_c = \frac{\gamma}{\pi} W \exp\left(-\frac{1}{\lambda}\right) \quad (37)$$

for  $q \rightarrow 0$ . As  $\tilde{\omega}_a(q=0)=0$  at all temperatures, the ‘‘softening’’ in this case means vanishing of the acoustic-phonon velocity  $v(q)$  at  $T=T_c$ ,

$$v(q) = \frac{\partial \tilde{\omega}_a(q)}{\partial q} \propto q, \quad (38)$$

as follows from Eq. (34). Thus, no matter how much the optical coupling constant is larger than the acoustic coupling constant, it is always the velocity of the acoustic phonon that becomes zero at  $T=T_c$ , whereas the optical-phonon frequency stays finite at this temperature,

$$\tilde{\omega}_o(q=0) = \omega_o \sqrt{\frac{\lambda_a}{\lambda}}. \quad (39)$$

The fact that at  $T_c$  the velocity of the acoustic phonon becomes zero while the optical-phonon frequency stays finite is a consequence of the mixing of the optical and acoustic phonons due to their interactions with electrons, which results in the repulsion between the frequencies of the two modes. Because of that, the optical and acoustic branches can never cross and the singularity at  $T_c$  always occurs in the lower, i.e., acoustic, branch. A similar effect takes place in some ferroelectrics, in which the sound velocity vanishes at the transition temperature because of the mixing of the soft mode, describing the ferroelectric displacement of ions to acoustic phonons.<sup>21</sup>

We also note that, at first sight, Eq. (37) resembles the result for the Peierls temperature obtained in Ref. 9. It should be kept in mind, however, that in that paper the various coupling constants  $\lambda_i$  correspond to contributions from scattering within different electron bands and are not associated with the presence of several phonon modes. The additive effect of the number of electron bands is implicit in our result through the fact that both  $\lambda_o$  and  $\lambda_a$  are proportional to  $N_F$ .

Finally, it is worthwhile to mention here that our results also hold if phonons of momentum  $q \sim 2k_F$  are included. Electron backscattering between different Fermi points is indicated by the dashed arrow in Fig. 2 and the accompanied lattice distortion resembles a Kekulé structure of the carbon nanotube lattice. We checked that this type of backscattering cooperates with the considered acoustic- and optical-phonon modes. This means that the opening of the Peierls gap may take place at an even higher critical temperature, Eq. (37), as  $\lambda$  is the sum of the three dimensionless electron-lattice coupling constants in this case.

#### IV. ELECTRICAL CONDUCTIVITY OF AN ARMCHAIR CARBON NANOTUBE

The acoustic phonons that correspond to a twist deformation of the nanotube lattice couple right- and left-moving electrons at each Fermi point. Since the velocity of the twistons is orders of magnitudes smaller than the Fermi velocity of electrons, these modes are always heavily thermally populated and, in contrast to the high-energy optical phonons, these phonons are effective at backscattering electrons. The

scattering of electrons on the acoustic phonons with the temperature-independent bare phonon dispersion has recently been used to explain the linear temperature dependence of the resistivity of an armchair carbon nanotube.<sup>18</sup> Here, we briefly reconsider the temperature dependence of the electrical conductivity  $\sigma(T)$ , taking into account the renormalization of the acoustic-phonon frequency due to the electron-phonon interactions.

The electrical conductivity for an armchair carbon nanotube is calculated using the Kubo formula

$$\sigma(T) = -\frac{4e^2v_F}{\pi} \int dk \tau_k \frac{\partial n_F[\varepsilon(k)]}{\partial k}, \quad (40)$$

where  $\tau_k$  is the electron transport lifetime, which depends on the electron wave vector  $k$ , and  $n_F[\varepsilon(k)]$  is the Fermi distribution with the linear electron energy dispersion  $\varepsilon(k) = v_F k$ . The factor 4 in Eq. (40) accounts for the spin degrees of freedom and the number of Fermi points  $N_F=2$ . The transport lifetime is calculated from the imaginary part of the electron self-energy describing the backscattering off the acoustic phonons:<sup>22</sup>  $\tau_k = 1/(4|\text{Im}\{\Sigma_{el}[k, \varepsilon(k)]\}|)$ . We take into account one-phonon scattering processes for which the expression of the electron self-energy becomes<sup>22</sup>

$$\begin{aligned} \Sigma_{el}(k, i\omega_m) &= -\frac{1}{L} \sum_q T \sum_{i\tilde{\omega}_m} |g_a|^2 D_a(q, i\tilde{\omega}_m) G(k+q, i\omega_m + i\tilde{\omega}_m), \end{aligned} \quad (41)$$

where  $\omega_m$  and  $\tilde{\omega}_m$  are, respectively, fermionic and bosonic Matsubara frequencies,  $q$  is the phonon momentum, and we set  $k_B=1$ . The Green’s function for the electron with energy dispersion  $\varepsilon(-k-q)$  is denoted by  $G(k+q, i\omega_m + i\tilde{\omega}_m)$ , while the dressed phonon propagator is denoted by  $D_a(q, i\tilde{\omega}_m)$ . It describes the acoustic phonons with renormalized frequency  $\tilde{\omega}_a(q)$  and is obtained from a diagonalization of the propagation matrix  $\mathcal{D}$  given by Eq. (30). The contribution of the optical phonons to the resistivity can be neglected for temperatures  $T \ll \tilde{\omega}_o$ . For  $\lambda_a \ll \lambda_o$  this inequality may not be fulfilled close to  $T_c$ , as the renormalized optical-phonon frequency Eq. (39) at  $T_c$  may then be small. However, since the optical phonon frequency is known to be as large as  $\omega_o \sim 2000$  K,<sup>23,24</sup> and assuming that  $\lambda_a$  and  $\lambda_o$  are of approximately the same order in armchair carbon nanotubes (see Sec. VII), no dramatic softening of the optical phonon is to be expected and the conductivity close to  $T_c$  is dominated by the electron backscattering off acoustic phonons.

It is straightforward to obtain the imaginary part of the retarded self-energy [ $i\omega_m \rightarrow \varepsilon(k) + i\delta$  and  $\delta \rightarrow 0$ ],

$$\begin{aligned} \text{Im}\{\Sigma_{el}[k, \varepsilon(k)]\} &= -\frac{\pi\lambda_a}{16} \int_{-\infty}^{+\infty} dq \frac{\omega_a^2}{\tilde{\omega}_a} [2n_B(\tilde{\omega}_a) + 1] \delta(2k+q), \end{aligned} \quad (42)$$

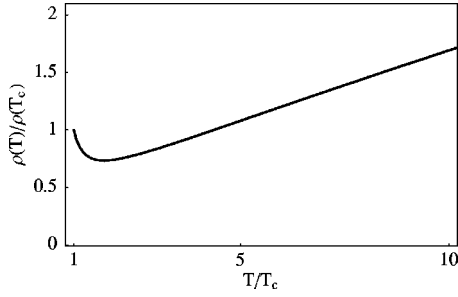


FIG. 7. Numerical calculation of the electrical resistivity  $\rho$  according to Eq. (44). The resistivity is plotted as a function of the temperature and the dimensionless electron-lattice couplings are chosen to be  $\lambda_a = \lambda_o = 0.05$ .

where  $n_B(\tilde{\omega}_a)$  is the Bose-Einstein distribution. In the derivation of this expression we used the fact that the velocity of acoustic phonons is much smaller than the Fermi velocity  $v(q) \ll v_F$ , and took elastic-scattering processes into account. Furthermore, since  $2n_B(\tilde{\omega}_a) + 1 \approx 2T/\tilde{\omega}_a$  for  $T \gg \tilde{\omega}_a$ , we finally obtain the transport lifetime

$$\tau_k = \frac{2}{\pi \lambda_a T} \left( \frac{\tilde{\omega}_a(2k)}{\omega_a(2k)} \right)^2. \quad (43)$$

In Fig. 7 we plot the temperature dependence of the electrical resistivity  $\rho(T) = \sigma(T)^{-1}$ , which is calculated numerically for  $T \geq T_c$  from

$$\rho(T) = \frac{\lambda_a \pi^2 T^2}{2e^2 v_F^2} \left[ \int dk \left( \frac{\tilde{\omega}_a(2k)}{\omega_a(2k) \cosh\left(\frac{v_F k}{2T}\right)} \right)^2 \right]^{-1}. \quad (44)$$

At temperatures  $T \gg T_c$ , the electrical resistivity Eq. (44) decreases linearly with the temperature,  $\rho(T \gg T_c) = \kappa_0 \lambda_a T$ , where  $\kappa_0 = \pi^2 / (8e^2 v_F)$ . However, close to  $T_c$ , due to the vanishing of the acoustic-phonon velocity at the critical temperature, the resistivity Eq. (44) strongly increases up to some finite value,  $\rho(T_c) \approx \kappa_0 \sqrt{2} (\lambda_a / \lambda)^2 T_c$ . This behavior is very similar to the one observed for bundles of single-wall carbon nanotubes,<sup>18</sup> where the crossover between the linear decrease and the sharp upturn of the electrical resistivity occur at  $T^* \sim 10 - 100$  K. In Sec. VII we discuss the relevance of phonon softening to this observed upturn, as well as the general possibility of observing the Peierls instability in carbon nanotubes.

## V. TOPOLOGICAL EXCITATIONS IN THE PEIERLS PHASE

We study the ordered Peierls state ( $T < T_c$ ) in the presence of optical- and acoustic-phonon modes. Because the lattice distortions, corresponding to the optical and acoustic phonons, are coupled due to electron-lattice interactions, two order parameters  $\Delta_a(x)$  and  $\Delta_o(x)$  should appear below the transition temperature. In the mean-field treatment of the lattice the total free energy of the model Eq. (20) is minimized with respect to the two order parameters. The solutions of the

resulting self-consistency equations have the following properties: (i) The sum of the optical and acoustic order parameters corresponds to a generalized order parameter

$$\Delta(x) = \Delta_o(x) + \Delta_a(x), \quad (45)$$

which satisfies the same Bogoliubov–de Gennes equations as the order parameter of the TLM model<sup>17</sup> with a single phonon mode, but with the dimensionless electron-lattice coupling constant  $\lambda = \lambda_a + \lambda_o$ , as given by Eq. (36). (ii) The optical ( $i = o$ ) and acoustic ( $i = a$ ) order parameters are proportional to  $\Delta(x)$ :

$$\Delta_i(x) = \frac{\lambda_i}{\lambda} \Delta(x). \quad (46)$$

It thus follows that the stationary minimal-energy lattice configuration of the continuum model Eq. (20) can be equally deduced from that of the Hamiltonian

$$H = \sum_s \int dx \Psi_s^\dagger(x) \left\{ \frac{v_F}{i} \sigma_3 \frac{\partial}{\partial x} + \Delta(x) \sigma_1 \right\} \Psi_s(x) + \frac{N_F}{\pi \lambda v_F} \int dx \Delta(x)^2 \quad (47)$$

in terms of the generalized order parameter  $\Delta(x)$  and the coupling constant  $\lambda$ . Here, we introduced the index  $s = (\sigma, n)$ , which is a combination of the electron's spin degrees of freedom  $\sigma = \pm 1$  and the number of Fermi points  $n = 1, \dots, N_F$ . In other words, an effective internal degeneracy  $N_d = 2N_F$  is ascribed to the electrons and each one-electron level can be occupied by up to  $N_d$  electrons. The advantage of relating Eq. (20) to Eq. (47) is that formally, Eq. (47) is equivalent to the Hamiltonian of the TLM model,<sup>17</sup> where electrons interact with one optical-phonon mode [ $\Delta(x) = \Delta_o(x)$ ] and  $N_F = 1$ . The solutions of this model can be used to study the ordered state of our model Eq. (20).

In particular, the value of the homogeneous solution  $\Delta(x) = \Delta_0$  at zero temperature is given by the mean-field result

$$\Delta_0 = W \exp\left(-\frac{1}{\lambda}\right) = \frac{\pi}{\gamma} T_c, \quad (48)$$

which coincides with the critical temperature Eq. (37) as obtained within the random-phase approximation. A homogeneous optical order parameter  $\Delta_o = \text{const}$  is a “frozen” phonon mode corresponding to a lattice deformation with out-of-phase bond-length dimerization in neighboring zigzag chains along the nanotube axis, as is shown in Fig. 8(a). On the other hand, for acoustic phonons,  $\Delta_a = \text{const}$  describes a static twist of the cylindrical nanotube lattice and corresponds to ionic displacements that grow linearly along the nanotube:  $u_a(x) = \tan(\theta)x$  ( $\theta$  is the twist angle). As is clear from Fig. 8(b), this distortion also leads to out-of-phase bond-length alternation in neighboring chains, explaining why the optical and acoustic modes cooperate in opening the Peierls gap. It should be stressed that the distortion  $\Delta_a = \text{const}$  is not a “frozen” phonon mode, as it would corre-

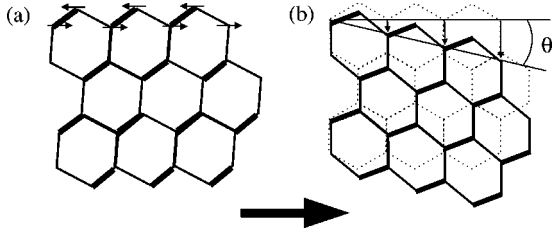


FIG. 8. (a) A homogeneous optical distortion  $\Delta_o = \text{const}$  results in a lattice deformation with out-of-phase bond-length dimerization in neighboring zigzag chains. (b) A homogeneous twist deformation  $\Delta_a = \text{const}$  corresponds to a shear of the graphene sheet, and leads to the same type of bond alternation. The thick arrow points in the direction along the nanotube axis.

spond to large deviations of ions from their equilibrium positions in the high-temperature phase.

Furthermore, as is known from the TLM model, kinks (solitons) in the order parameter, corresponding to a change of sign of the lattice dimerization along the chain, constitute an interesting class of excitations.<sup>16,17</sup> The analytical expression for the kink is given by<sup>17</sup>

$$\Delta(x) = \Delta_0 \tanh(x/\xi_0), \quad (49)$$

where  $\xi_0 = v_F/\Delta_0$  is the correlation length. It is easy to verify that the configuration Eq. (49) for the generalized order parameter in our model corresponds to the optical and acoustic lattice distortions given by

$$\begin{aligned} u_o(x) &= \bar{u}_o \tanh(x/\xi_0), \\ u_a(x) &= \bar{u}_a \ln \cosh(x/\xi_0). \end{aligned} \quad (50)$$

Near the kink, which we call a solitwiston, both the lattice dimerization, described by  $u_o(x)$ , and the derivative of  $u_a(x)$  change sign.

In the TLM model ( $u_a = 0$ ), the soliton is the minimal-energy lattice configuration in a chain (of connected carbon rings) with antiperiodic boundary conditions on the atomic shifts  $u_o(x+L) = -u_o(x)$  ( $L$  is the system length). The corresponding discrete model is that of a closed chain with an odd number of lattice sites, where the dimerization  $\Delta_o$  changes sign around the soliton position. If the number of lattice sites in the closed chain is even, however, the minimal-energy lattice configuration contains no soliton, corresponding to the continuum model for a chain with periodic boundary conditions [ $u_o(x+L) = u_o(x)$ ]. The situation is different in the presence of a twist ( $u_a \neq 0$ ): For a homogeneous ground-state lattice configuration with acoustic distortion  $u_a(x) = \tan(\theta)x$ , periodic boundary conditions require that

$$\frac{\partial u_a(x)}{\partial x} = \tan \theta = n_w \frac{C}{L}. \quad (51)$$

Here, we introduced an integer winding number  $n_w$ , while  $C$  and  $L$  denote, respectively, the circumference and the length of the carbon nanotube. In other words, the optimal value of the twist angle  $\theta$ , which follows from Eqs. (48) and (46), has

to be equal to a value of a discrete set that is characterized by  $n_w$ . We note that lattice configurations with different winding numbers belong to different topological classes that classically cannot be continuously transformed into each other. The trivial solution  $n_w = 0$  corresponds to a ground-state lattice configuration with  $\Delta = 0$ , while the condition Eq. (51) for a homogeneous ground-state lattice configuration with  $\Delta = \text{const}$  is most easily realized in long carbon nanotubes for which  $C/L \rightarrow 0$ . To gain energy from the lattice distortion and, at the same time, to satisfy the periodic boundary conditions  $\int_0^L dx \Delta_a(x) = 0$ , it is possible that an inhomogeneous ground-state lattice configuration becomes energetically more favorable. Then,  $u_a(x)$  has to change sign at least two times along the electronic chain and the minimal-energy lattice configuration contains one solitwiston and one antisolitwiston.

It follows from Eq. (47) that the creation energy  $\mu$  of a solitwiston is formally the same as for the usual soliton in the TLM model taking into account the internal electron degeneracy  $N_d$ :

$$\mu = \frac{N_d \Delta_0}{\pi} = \frac{4\Delta_0}{\pi}. \quad (52)$$

The dynamical properties of the kinks in our model are, however, quite different from those in the TLM model with  $u_a = 0$ . In the latter, the soliton can propagate with velocity  $v$  along the chain, without changing its profile. This results from the independence of the soliton energy of its position and the fact that the kinetic-energy density of the moving soliton  $u_o(x,t) = \bar{u}_o \tanh[(x-vt)/\xi_0]$  decays exponentially at distances larger than the correlation length  $\xi_0$  away from the soliton position. Thus, the mass of the soliton is finite and for *transpolyacetylene* was estimated to be  $\sim 6m_e$  (with  $m_e$  the electron mass).<sup>16</sup> On the other hand, the motion of the kink in the model with acoustic phonons ( $u_o = 0$ ) would result in a constant kinetic-energy density at distances larger than  $\xi_0$  from the kink. This follows from the substitution of  $u_a(x)$  in Eq. (50) by  $u_a(x-vt)$  and a calculation of the kinetic energy  $E_s = (M_s/2)v^2$ . We then find for an armchair carbon nanotube consisting of carbon atoms with mass  $M_C$

$$M_s \propto M_C \int_{-L/2}^{L/2} \frac{dx}{a} \tanh\left(\frac{x}{\xi_0}\right)^2 \propto M_C \frac{L}{a} \quad (53)$$

and, thus, that the mass of a kink is proportional to the system length  $L$ . It follows that isolated solitwistons cannot propagate. This relates to the fact that a translation of the solitwiston configuration Eq. (50) changes the coordinates at the boundaries of the system, so that its shift induces a motion of the entire system. Solitwistons can propagate without affecting the boundaries of the system only together with antisolitwistons and the mass of such a pair is proportional to its pair size  $R (\gg \xi_0)$ .

We now turn to a discussion of the solitwiston's spin-charge relations: Similar to the case of *transpolyacetylene*, the single-particle electronic spectrum of the armchair carbon nanotube follows from Eq. (47) to consist of a continuum of plane-wave conduction- and valence-band states

that are separated by an energy gap  $2\Delta_0$ . The presence of a solitwiston Eq. (49) gives rise to a localized midgap state that can be either unoccupied or occupied by up to  $N_d=4$  electrons. The solitwiston's spin-charge relations differ from those of the soliton in *transpolyacetylene*, where the midgap state of the soliton can be occupied by only  $N_d=2$  electrons ( $N_F=1$ ), and are, instead, equivalent to those expected for the topological excitation in polyynes.<sup>25</sup> In the (undoped) armchair carbon nanotube the neutral solitwiston ( $Q=0$ ) can have spin  $S=0$  or  $S=1$  since two electrons occupy the midgap states at the two Fermi points. The spin-charge relations of the charged solitwiston in armchair carbon nanotubes are seen to be quite usual, in contrast to the exotic spin-charge relations of solitons in *transpolyacetylene*.<sup>16</sup>

We should mention here that the model Eq. (47) also predicts the existence of a nontopological excitation corresponding to a bound solitwiston-antisolitwiston pair. In analogy to the polaron in conjugated polymers,<sup>16</sup> this excitation is called a *polartwiston* as it describes a local indentation of the acoustic and optical lattice distortions in the carbon nanotube. The energy spectrum for this type of excitation contains two localized intragap states with energies  $\pm \varepsilon$  depending on the electron occupancy  $n_{\pm}$  of the intragap states. Both the creation energy of the polartwiston

$$\mu_p = 2\mu \sin \phi \quad (54)$$

and the maximal change of the generalized order parameter associated with the local indentation around the polartwiston position

$$\delta\Delta = (2 \cos \phi - 1)\Delta_0 \quad (55)$$

depend on the electron occupancy of the intragap states, which is hidden in the definition of the angle

$$\phi = \frac{\pi}{2} \left( 1 + \frac{n_+ - n_-}{N_d} \right). \quad (56)$$

The spin-charge relations of a polartwiston are summarized as follows: A polartwiston with charge  $Q = \pm e$  or  $Q = \pm 3e$  has spin  $S=1/2$ , while a polartwiston that is neutral or has a charge  $Q = \pm 2e$  can have spin  $S=0$  or  $S=1$ . Note that the neutral polartwiston in the system with internal degeneracy  $N_d=4$  does not have a counterpart in the  $N_d=2$  system. Its creation energy  $\mu_p = \sqrt{2}\mu$  is less than that of a neutral solitwiston-antisolitwiston pair. However, since two neutral polartwistons are unstable and decay into a solitwiston-antisolitwiston pair, the latter will be the lowest-lying thermal excitation in armchair carbon nanotubes. It is also interesting to note that the creation energy of a polartwiston with charge  $Q = \pm e$  in the  $N_d=4$  system is smaller than that of a solitwiston  $\mu_p \approx 0.77\mu$ . This difference with the  $N_d=2$  system has important consequences for the creation of topological excitations as will be further discussed in the next section.

## VI. NUMERICAL SIMULATION: ELASTIC SPRING MODEL

In this section we present the results of numerical simulations which we performed to study the appearance of solitwistons and polartwistons in the Peierls state of armchair carbon nanotubes with different types of boundary conditions on the atomic shifts. We impose free boundary conditions to describe the straight carbon nanotube with open ends, while periodic boundary conditions correspond to the carbon nanotube of seamless toroidal shape.<sup>26</sup>

The potential energy of the hexagonal nanotube lattice  $U$  is calculated within a discrete elastic spring model where carbon atoms are connected by ‘‘springs’’ which are characterized by elastic spring constants. We derive an expression of  $U$  under the assumption that it depends only on the change in the distance between the carbon atoms. The potential energy consists of three terms  $U = U_{AB} + U_{AA} + U_{BB}$ , where  $U_{AB}$  refers to the coupling between carbon atoms of the two different sublattices  $A$  and  $B$ , while  $U_{AA}$  and  $U_{BB}$  denote the potential lattice energy within sublattices  $A$  and  $B$ , respectively. Explicitly, we have

$$U_{ij} = \frac{1}{2} \sum_{l,m} K(R_{lm}) ([\vec{u}_i(\vec{x}_l) - \vec{u}_j(\vec{x}_m)] \cdot \hat{R}_{lm})^2, \quad (57)$$

where  $K(R_{lm})$  denotes the spring constant as a function of the distance  $R_{lm}$  between two carbon atoms that are located at sites  $\vec{x}_l$  and  $\vec{x}_m$  in sublattices  $i$  and  $j$ , respectively, while  $\hat{R}_{lm}$  is the corresponding unit vector. The displacement of a carbon atom from its equilibrium position at  $\vec{x}_l$  in the  $i$ th sublattice is denoted by  $\vec{u}_i(\vec{x}_l)$ .

The summation over  $l, m$  in Eq. (57) accounts for all pairs of carbon atoms in sublattices  $i$  and  $j$ . In practice we will calculate the potential lattice energy Eq. (57) accounting for a carbon atom's three nearest neighbors by three different spring constants  $K_1$ ,  $K_2$ , and  $K_3$ . Furthermore, as we explained in Sec. II, it is sufficient to consider the two-dimensional atomic displacement vector in the  $i$ th sublattice to be a function of the  $x$  coordinate along the nanotube axis only,  $\vec{u}_i(x=na/2) = [X_i(na/2), Y_i(na/2)]^T$ . The armchair nanotube lattice is again considered as consisting of  $N$  connected rings at a distance  $a/2$  along the nanotube axis (see Fig. 1), such that a lattice configuration is completely determined by the set  $\{\hat{u}\} \equiv \{\vec{u}_A(na/2), \vec{u}_B(na/2)\}$  of atomic displacements.

We compute the minimal-energy lattice configuration using a steepest-descent algorithm, where we start from a randomly chosen lattice configuration and calculate the total ground-state energy,  $E[\{\hat{u}\}] = \langle 0 | H_{arm} | 0 \rangle + U$ , for the electronic ground state  $|0\rangle$  of the discrete two-leg ladder Hamiltonian Eq. (9) associated with this lattice configuration. Next, we compute the gradient

$$\vec{\nabla} E_{n,i} = \frac{\delta E[\{\hat{u}\}]}{\delta \{\vec{u}_i(na/2)\}} \quad (58)$$

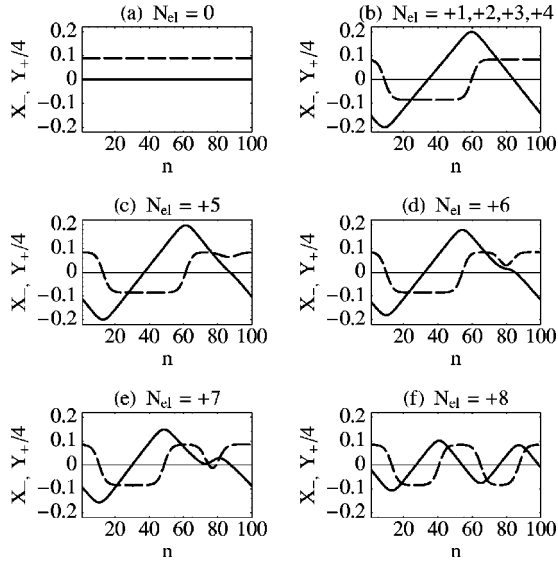


FIG. 9. Minimal-energy lattice configuration of the armchair carbon nanotube in the Peierls phase for periodic boundary conditions imposed on the shifts  $X_-$  (dashed line) and  $Y_+$  (solid line).  $N_{el}$  denotes the number of electrons that is added to the half-filled system.

in each ring  $n$  for both sublattices  $i=A,B$  leaving the atomic displacements in all the other rings unchanged. We determine from the sign of  $\vec{\nabla} E_{n,i}$  in which direction the atomic displacement vector  $\vec{u}_i(na/2)$  is to be shifted such that  $E[\{\hat{u}\}]$  is decreased. In this way, we obtain a new lattice configuration  $\{\hat{u}'\}$  which is only accepted if the total ground-state energy  $E[\{\hat{u}'\}] < E[\{\hat{u}\}]$ . The same procedure is repeated until the gradient Eq. (58) is equal to zero within the required accuracy of the computation.

We now turn to the discussion of the results for the minimal-energy lattice configurations, which are presented in terms of the shifts

$$Y_+ = \frac{1}{\sqrt{2}}(Y_A + Y_B), \quad X_- = \frac{1}{\sqrt{2}}(X_A - X_B), \quad (59)$$

in Fig. 9 and Fig. 11 (below), respectively, for periodic and free boundary conditions. To obtain a qualitative picture of the Peierls state for a general armchair carbon nanotube the precise values of the parameters involved ( $N_l$ ,  $t_{\parallel}$ ,  $\alpha_{\parallel}$ ,  $K_1$ ,  $K_2$ , and  $K_3$ ) are not important and are, instead, chosen to satisfy the following two convenient conditions: (i) For a system of  $N=100$  rings, the correlation length is much smaller than the system size  $\xi_0 = v_F/\Delta_0 \ll Na/2$ . (ii) The coupling between the shifts  $Y_+$  and  $X_-$  is negligibly small, so that the numerical results are directly related to the corresponding acoustic and optical order parameters by

$$\Delta_a \propto \frac{\partial}{\partial x} Y_+, \quad \Delta_o \propto X_- \quad (60)$$

[see Eqs. (19) and (17)].

We first discuss the results for periodic boundary conditions which are summarized in Fig. 9. At half-filling (a), we

obtain  $Y_+ = 0$  and a finite value for  $X_-$ , corresponding to a relative shift of the two triangular sublattices  $A$  and  $B$ . The absence of a twist in the ground state, which is in obvious contradiction with the result of the continuum model Eq. (47), is a finite-size effect: The uniform twist is simply incompatible with the periodic boundary conditions for the given carbon nanotube length and model parameters. In Fig. 9(b) we show the effect of doping on the lattice configuration [Fig. 9(a)] by adding  $N_{el} = 1, \dots, 4$  electrons to the initially half-filled system. As we discussed in Sec. V, for an additional electron the creation of a polartwiston is, in principle, energetically more favorable than the creation of a solitwiston. However, since in the finite chain [Fig. 9(a)] there is no twist at half-filling, the energy is minimized by creation of a solitwiston-antisolitwiston pair [Fig. 9(b)]. This is a consequence of the condition that in order to create a polartwiston the sign of  $u_a(x)$  has to be different to the left and the right of the polartwiston position  $u_a(x \ll x_0) = -u_a(x \gg x_0)$ , which cannot be satisfied in the lattice configuration [Fig. 9(a)] with  $Y_+ = 0$ . As the antibonding superposition of the midgap states of the two solitwistons can accommodate up to  $N_d = 4$  electrons, the lattice configuration [Fig. 9(b)] remains the same for  $N_{el} = 2, 3, 4$ . Then, on adding the fifth up to seventh electron, a charged polartwiston appears in the carbon nanotube lattice [see Figs. 9(c)–9(e)]. This excitation distorts the lattice locally with an indentation that depends on the number of added electrons and which we find to be even in quantitative agreement with the relative change calculated according to Eqs. (55) and (56). Finally, we plot in Fig. 9(f) the minimal-energy lattice configuration obtained with eight extra electrons for which the periodic boundary conditions require a second solitwiston-antisolitwiston pair to appear.

The appearance of topological excitations in the minimal-energy lattice configuration depends on the imposed boundary conditions for the atomic shifts. This can be readily understood within the two-leg ladder model and is illustrated in Fig. 10. If periodic boundary conditions are imposed on the shifts, the number  $N$  of rings in the armchair carbon nanotube has to be even. The out-of-phase dimerization of the minimal-energy lattice configuration is depicted by thick and thin lines in the two-leg ladder. No topological excitations are present if the twist deformation is homogeneous with  $\tan \theta = n_w C/L$  [Fig. 10(a)], while otherwise the lattice configuration contains (for a sufficiently large system) a solitwiston-antisolitwiston pair [Fig. 10(b)]. The latter configuration is schematically shown by four unpaired electrons which give rise to the two doubly occupied midgap states. If, on the other hand, the boundary conditions on the shifts are free, the number  $N$  of rings in the armchair carbon nanotube can be either even or odd. The corresponding minimal-energy lattice configurations are then quite similar in both cases, since the system has the freedom to minimize its energy by a relative shift of the two triangular sublattices  $A$  and  $B$  against each other and by a static twist deformation. This is depicted in Figs. 10(c) and 10(d) by the out-of-phase dimerization in the two-leg ladder. It is, however, important to notice the difference between periodic and free boundary conditions. For the latter, the half-filled system contains two unpaired electrons, independent of whether  $N$  is even or odd,

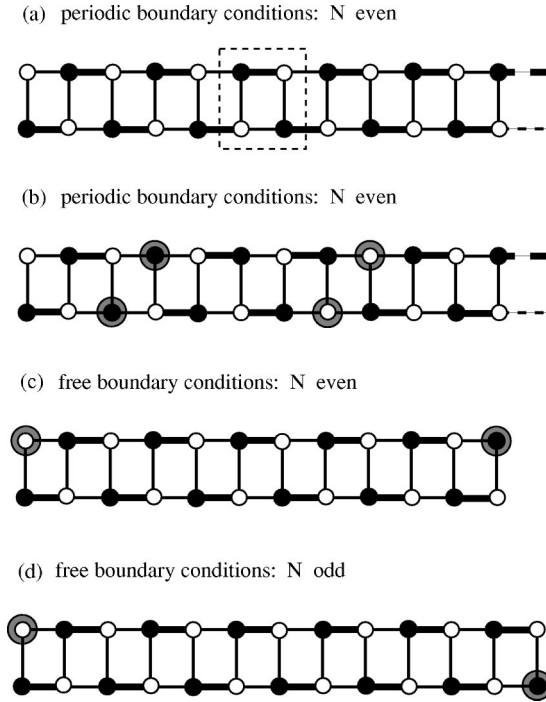


FIG. 10. The minimal-energy lattice configuration for periodic and free boundary conditions on the lattice distortions. The dashed rectangle indicates the unit cell of the lattice that consists of the two sublattices “●” and “○”. An unpaired electron is indicated by the shaded circle. See the text for details.

which are located at the left and right ends of the system. These electrons give rise to edge states that appear in the middle of the Peierls gap. On doping the system the first two electrons will occupy the midgap electronic level associated with the two edge states and, therefore, the lattice configuration will remain unchanged.

That this picture is, in fact, correct can be seen in Fig. 11 where we plot the results of numerical simulations for free boundary conditions on the shifts. The minimal-energy lattice configuration of the half-filled system [Fig. 11(a)] is, as expected, characterized by a lattice dimerization associated with a relative shift of the two triangular sublattices ( $X_- = \text{const}$ ) and a homogeneous twist deformation ( $Y_+ \propto x$ ). This lattice configuration does not change when the first and second electrons are added in Figs. 11(b) and 11(c). Inspection of the electron energy spectrum reveals that the two added electrons occupy, in fact, a midgap state associated with the edge states that arise as a consequence of the imposed boundary conditions. A relaxation of the lattice is only seen on adding the third electron to the system [Fig. 11(d)]. As pointed out at the end of Sec. V, the creation of a polartwiston with charge  $Q = -e$  is energetically more favorable than the creation of a solitwiston. This polartwiston is seen to be located at the (right) system boundary, where the presence of the edge state gives rise to a level splitting that minimizes the system’s total energy. In Fig. 11(e), we plot the minimal-energy lattice configuration containing four extra electrons. A charged solitwiston with  $Q = -2e$  is now seen to be located in the middle of the armchair nanotube lattice and, beside the two completely occupied edge states,

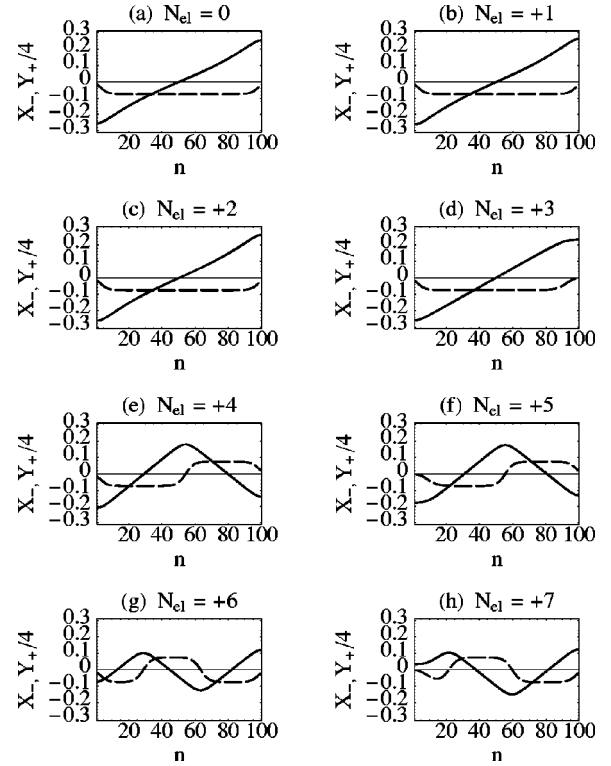


FIG. 11. Minimal-energy lattice configuration of the armchair carbon nanotube in the Peierls phase for free boundary conditions imposed on the shifts  $X_-$  (dashed line) and  $Y_+$  (solid line).  $N_{el}$  denotes the number of electrons that is added to the half-filled system.

the midgap state associated with this solitwiston is completely occupied by four electrons. Therefore, on adding the fifth electron [Fig. 11(f)], again a charged polartwiston with  $Q = -e$  is formed that is located at the (left) boundary. This is similar to the situation in Fig. 11(d) and together with Figs. 11(g) and 11(h) for, respectively, six and seven extra electrons we obtain the following general pattern: (i) A charged polartwiston ( $Q = -e$ ) is located at the system’s boundary if the number  $N_{el}$  of added electrons is odd and larger than two. (ii) The number of charged solitwistons ( $Q = -2e$ ) increases by one if the number  $N_{el}$  of added electrons is even and larger than two.

## VII. DISCUSSION

As we mentioned already, the Peierls transition is commonly believed to be irrelevant for carbon nanotubes, because the transition temperature  $T_c$  is estimated to be negligibly small. This smallness results from the fact that  $T_c$  depends exponentially on the electron-lattice coupling constant  $\lambda$  [Eq. (37)] and  $\lambda$  is inversely proportional to the number of zigzag chains around the circumference of the armchair carbon nanotube. We note, however, that while usually  $\lambda$  is taken to be the coupling with just one optical-phonon mode, we have seen above that optical and acoustic modes cooperate in the opening of the Peierls gap:  $\lambda = \lambda_o + \lambda_a$  [Eq. (36)]. As a result of the exponential behavior of  $T_c$ , this additive dependence on the two coupling constants may

greatly enhance  $T_c$ , especially for nanotubes with  $N_l$  small. In this section, we present estimates for  $\lambda$  and  $T_c$ , we address the relevance of the Peierls instability to experiments, and we discuss the role of electron-electron interactions.

To estimate  $\lambda_o$  and  $\lambda_a$ , we use the elastic spring model considered in Sec. VI. The calculation of the coupling constants as a function of the three spring constants  $K_1$ ,  $K_2$ , and  $K_3$  is given in the Appendix. For the optical-phonon mode we obtain

$$\lambda_o = \frac{12\alpha_{\parallel}^2 \sin\left(k_F \frac{a}{2}\right)}{\pi t_{\parallel} \omega_o^2 M_C N_l}, \quad (61)$$

where  $M_C$  is the mass of the carbon atom. Using typical values for the electron hopping amplitudes along and perpendicular to the nanotube axis  $t_{\parallel} \approx t_{\perp} \approx 2.5$  eV, the electron-lattice coupling,  $\alpha_{\parallel} \approx 4.1$  eV Å<sup>-1</sup>, and the experimentally and numerically determined value for the optical-phonon frequency  $\omega_o \approx 0.18$  eV,<sup>23,24</sup> we find  $\lambda_o \approx 0.24/N_l$ . For the dimensionless electron-lattice coupling of the acoustic-phonon mode we obtain

$$\lambda_a = \lambda_o \frac{27K_3^2 a^2}{16M_C^2 \omega_o^2 v_0^2}, \quad (62)$$

which is finite only for a nonzero spring constant  $K_3$ . This reflects the fact that a twist distortion depends crucially on the elastic coupling between distant atomic neighbors, as also the corresponding twist angle  $\theta$  is related to the derivative of the distortion amplitude  $\tan \theta = [u_a(x+a) - u_a(x)]/a$ .

In order to estimate the value of  $\lambda_a$ , we first have to determine the values of the three spring constants. Two conditions are given by the optical-phonon frequency Eq. (A7) and the sound velocity Eq. (A8), which we require to yield the experimentally and numerically obtained values  $\omega_o \approx 0.18$  eV (Refs. 23 and 24) and  $v_0 \approx 14$  km/s,<sup>14,24</sup> respectively. A third condition is imposed by fitting the value of the acoustic-phonon frequency at  $q = \pi/a$ , where the acoustic branch deviates from its linear  $q$  dependence and the frequency is known to be approximately  $\omega_a(\pi/a) \approx 0.07$  eV.<sup>14,24</sup> The expression for  $\omega_a(\pi/a)$  in terms of the three coupling constants is given by Eq. (A9). In this way we obtain  $K_1 \approx 25$  eV Å<sup>-2</sup>,  $K_2 \approx 1.1$  eV Å<sup>-2</sup>, and  $K_3 \approx 8.1$  eV Å<sup>-2</sup>. It thus turns out that  $K_3 > K_2$  is required in order to fulfill all three conditions. This counterintuitive result probably is a consequence of the fact that our model with only three spring constants is the minimal model that leads to a finite value of  $\lambda_a$  and should be viewed as an effective description of the complicated lattice dynamics. In fact, it is known that more involved force-constant models are required to accurately describe the phonon spectrum of the graphene sheet and carbon nanotubes.<sup>24,27</sup>

To maintain a consistent analysis, we proceed by using the above values for  $K_1$ ,  $K_2$ , and  $K_3$ . We then find from Eq. (62) that  $\lambda_a \approx \lambda_o/4$ , leading to  $\lambda = \lambda_o + \lambda_a \approx 0.3/N_l$ . It then follows from Eq. (37) with  $W = 10$  eV that for large nano-

tubes ( $N_l \sim 10$ ),  $T_c$  is indeed negligibly small ( $< 10^{-9}$  K) and the associated softening of the acoustic phonons, leading to the upturn of the resistivity at low temperature (Fig. 7), will not be relevant to the explanation of the observed upturn for these large nanotubes.<sup>18</sup> In fact, it has been shown that for such large-radius nanotubes, the temperature dependence of the resistivity can be well explained using a Luttinger model that describes the forward scattering due to electron-electron interactions, in addition to electron scattering on acoustic phonons, without accounting for possible phonon softening.<sup>4,5,28,29</sup>

At the same time, it is clear that for nanotubes with smaller values of  $N_l$ , the Peierls instability becomes more important. Recent examples of small-radius nanotubes that have been prepared experimentally are those with  $N_l \sim 4$ ,<sup>30</sup> the possible technological interest in such narrow nanotubes has been emphasized in Ref. 31. While, to the best of our knowledge, transport measurements on such narrow nanotubes have not yet been reported, it is of interest to assess the relevance of the Peierls instability for them. Using the above estimate  $\lambda \approx 0.3/N_l$ , we arrive at  $T_c \sim 0.1$  K for  $N_l = 4$  and  $T_c \sim 3$  K for  $N_l = 3$ . The steep increase relative to the case  $N_l = 10$  reflects the exponential dependence on  $\lambda$ . This same dependence makes  $T_c$  extremely sensitive to the precise value of  $\lambda$  and calls for caution, as the prefactor 0.3 in our expression for  $\lambda$  is only an order-of-magnitude estimate. To illustrate this, we note that if this factor is increased by 50%, the above estimates change to  $T_c \sim 9$  K for  $N_l = 4$  and  $T_c \sim 80$  K for  $N_l = 3$ . These numbers clearly indicate that the Peierls transition and the associated phonon softening may indeed be relevant for small-radius carbon nanotubes.

From the above discussion, it is also clear that the accurate determination of the electron-phonon coupling constants is of paramount importance when assessing the effect of the electron-lattice coupling in detail. While here we have given theoretical estimates for  $\lambda_a$  and  $\lambda_o$ , one may, in principle, also attempt to determine them from the resistivity curve. As we have found in Sec. IV,  $\lambda_a$  determines the slope of  $\rho(T)$  at high  $T$ , while  $T_c$  depends on  $\lambda = \lambda_a + \lambda_o$ . The problem in using this approach lies in our neglect of electron-electron interactions. Both forward scattering (Luttinger model<sup>29</sup>) and umklapp scattering, modeled by the on-site Hubbard model at half filling,<sup>6,7</sup> affect the shape of the resistivity curve. In particular, the contribution of umklapp scattering to the resistivity is also expected to result in a linear  $T$  dependence at temperatures larger than the charge gap  $E_g$ , associated with double occupation of a lattice site.<sup>6</sup> Although its contribution to the slope of the resistivity in the regime of linear  $T$  dependence vanishes as  $1/N_l^2$ ,<sup>6</sup> while electron-phonon interaction enters the slope through  $\lambda_a \propto 1/N_l$ , it is to be expected that attributing the slope to either one of the two scattering mechanisms alone will be impossible. We finally note that the charge gap arising in the Hubbard model gives rise to an activated behavior of the resistivity for  $T < E_g$ ,<sup>6</sup> which may be hard to distinguish from the upturn associated with phonon softening.

We conclude that unequivocal evidence for the occurrence of the Peierls transition in narrow carbon nanotubes is prob-

ably hard to obtain from measuring the electrical resistivity alone. Other experimental evidence could be provided by observing the vanishing of the phonon velocity at  $T_c$  (as has been done for the ferroelectric transition,<sup>21</sup> but not, to our best knowledge, for small-radius nanotubes yet) and by using microscopic and spectroscopic techniques to directly observe a twist deformation of an armchair carbon nanotube.<sup>19</sup> Similar techniques can, in principle, be used to probe the energies and shapes of the intragap states associated with solitwistons and polartwistons that occur in the Peierls phase, as introduced in Sec. V.

### VIII. SUMMARY AND CONCLUSIONS

An interesting feature of the Peierls scenario in the presence of both optical and acoustic phonons is that independent of the electron-lattice coupling constants the acoustic-phonon velocity vanishes at the critical temperature, whereas the optical-phonon frequency remains finite. In contrast to the conventional Peierls scenario, in which the optical phonon softens at the critical temperature in the absence of acoustic phonons, a level repulsion takes place between the optical- and acoustic-phonon modes due to their coupling by electron-hole excitations. In this way, the acoustic-phonon velocity is reduced to zero at the temperature  $T_c$  which is higher than the critical temperature of the conventional Peierls transition. Structural phase transitions resulting from electron-lattice interactions are of broad interest and our theory is not limited to one particular system. In fact, back-scattering due to acoustic phonons always occurs if the size of the system's unit cell is the same above and below the transition temperature  $T_c$ . The phonon wave vector is only conserved up to a multiple of  $2k_F$  in this case and optical- and acoustic-phonon modes of the same symmetry cooperate in the opening of the Peierls gap. In this paper we considered an armchair carbon nanotube where the unit cell contains two carbon atoms above and below  $T_c$  due to its zigzag-chain structure. The Peierls state contains both a static twist of the carbon nanotube along its axis and a lattice dimerization due to the relative shift of the two triangular sublattices in the carbon nanotube.

While we have attempted to reach more than just a qualitative picture of this Peierls transition and its consequences, it should be stressed that our quantitative predictions have large error bars. This is a consequence of the fact that quantities of interest, like the transition temperature, depend exponentially on the electron-lattice coupling constants involved, which are hard to estimate with high precision. In addition, the interactions with other carbon nanotubes or with the substrate may complicate the situation in practice. A link was made to experiments on carbon nanotubes by calculating the temperature dependence of the electrical resistivity due to electron scattering on acoustic phonons with renormalized frequency. We have found that the softening of the acoustic phonons close to  $T_c$  gives rise to an upturn in the electrical resistivity. This upturn will only be observable for small-radius carbon nanotubes and in general competes with similar upturns that derive from various electron-

electron scattering mechanisms. More generally, electron-electron interactions make it hard to estimate the electron-phonon coupling constants from temperature-dependent transport measurements alone.

We have studied the occurrence of topological excitations, solitwistons and polartwistons, in the ordered phase of an armchair carbon nanotube. We find that the electronic energy spectrum of the minimal-energy lattice configuration depends qualitatively on the applied boundary conditions (periodic and free), as can be understood in terms of the two-leg ladder model. It follows that the appearance of solitwistons and polartwistons is qualitatively different for the two types of boundary conditions. As carbon nanotubes can be examined individually and also exist in a seamless toroidal shape,<sup>26</sup> it will be an interesting challenge to use microscopy and spectroscopy techniques to probe the energies and shapes of the intragap states associated with solitwistons and polartwistons.

### ACKNOWLEDGMENTS

We gratefully acknowledge financial support from the Stichting Fundamenteel Onderzoek der Materie (FOM).

### APPENDIX

We calculate the couplings  $\lambda_a$ ,  $\lambda_o$  and the frequency  $\omega_a(\pi/a)$  within the elastic spring model of Sec. VI in terms of the spring constants  $K_1$ ,  $K_2$ , and  $K_3$ . For this purpose we write Eq. (57) using the Fourier representation of the atomic displacement Eq. (1),

$$\vec{u}_i(\vec{x}_i) = \frac{1}{\sqrt{N_i}} \sum_{\vec{q}} e^{i\vec{q}\cdot\vec{x}_i} [X_i(\vec{q}), Y_i(\vec{q})]^T, \quad (\text{A1})$$

where  $N_i$  is the number of sites in the  $i$ th sublattice and  $N_A = N_B$  in armchair carbon nanotubes. Let us choose the origin of the  $i$ th sublattice to be located at  $\vec{x}_i = 0$  from where we measure the distance to the  $m$ th atom in sublattice  $j$  by  $\vec{R}_m = |\vec{R}_m|(\cos \theta_m, \sin \theta_m)^T$ . If we combine the Fourier components of the atomic displacements in a single vector

$$\vec{u}(\vec{q}) = [X_i(\vec{q}), Y_i(\vec{q}), X_j(\vec{q}), Y_j(\vec{q})]^T, \quad (\text{A2})$$

we obtain Eq. (57) in the form  $U_{ij} = \frac{1}{2} \sum_{\vec{q}} \vec{u}(\vec{q})^\dagger \hat{K}_{ij} \vec{u}(\vec{q})$ . The matrix elements  $\hat{K}_{ij} = (k_{\alpha\beta})_{ij}$  (with  $\alpha, \beta = 1 \dots 4$ ) are given by

$$k_{11} = k_{33} = \sum_m K(R_m) \cos^2 \theta_m,$$

$$k_{22} = k_{44} = \sum_m K(R_m) \sin^2 \theta_m,$$

$$k_{12} = k_{21} = k_{34} = k_{43} = \sum_m K(R_m) \cos \theta_m \sin \theta_m,$$

$$k_{13}=k_{31}^*=-\sum_m K(R_m)e^{i\vec{q}\cdot\vec{R}_m}\cos^2\theta_m,$$

$$k_{14}=k_{41}^*=k_{23}=k_{32}^*=-\sum_m K(R_m)e^{i\vec{q}\cdot\vec{R}_m}\cos\theta_m\sin\theta_m,$$

$$k_{24}=k_{42}^*=-\sum_m K(R_m)e^{i\vec{q}\cdot\vec{R}_m}\sin^2\theta_m. \quad (\text{A3})$$

We now disregard the transverse momentum component in the matrix elements Eq. (A3) and write  $\vec{q}\cdot\vec{R}_m=qR_m\cos\theta_m$ , where  $q$  denotes the momentum in the direction along the nanotube axis. Furthermore, it is convenient to use a transformation  $\hat{U}$  with  $\hat{U}^\dagger\hat{U}=1$ , such that the vector with the Fourier components of the atomic displacements Eq. (A2) becomes with Eq. (59)

$$\vec{u}(\vec{q})\rightarrow\vec{\mathcal{R}}_q=\hat{U}\vec{u}(\vec{q})=(X_+,Y_+,X_-,Y_-)^T. \quad (\text{A4})$$

The potential lattice energy Eq. (57) takes the form  $U=\frac{1}{2}\sum_q\vec{\mathcal{R}}_q^\dagger\hat{\kappa}_q\vec{\mathcal{R}}_q$  with  $\hat{\kappa}_q\equiv\hat{U}(\hat{K}_{AB}+\hat{K}_{AA}+\hat{K}_{BB})\hat{U}^\dagger$ . We note that  $U$  contains the matrix elements Eq. (A3) and is, thus, still valid for all values of  $q$ .

In the limit of long wavelengths  $q\rightarrow 0$ , we expand the exponentials in Eq. (A3) up to second order in  $q$  and obtain the matrix  $\hat{\kappa}_q$  in the form

$$\hat{\kappa}_q=\frac{a}{2}\begin{pmatrix} q^2\beta_x & 0 & 0 & iq\delta_y \\ 0 & q^2\beta_y & -iq\delta_x & 0 \\ 0 & iq\delta_x & \alpha_x+q^2\gamma_x & 0 \\ -iq\delta_y & 0 & 0 & \alpha_y+q^2\gamma_y \end{pmatrix}. \quad (\text{A5})$$

As expected, the potential lattice energy  $U$  is formally identical to the potential lattice energy in the Hamiltonian  $H_{lat}$

given in Sec. II. In terms of the three spring constants the parameters are given by

$$\alpha_x=\alpha_y=\frac{3}{2a}(K_1+K_3),$$

$$\beta_x=3\beta_y=\frac{9a}{2}K_2+\frac{3a}{2}\left(\frac{1}{4}K_1+K_3\right),$$

$$\gamma_x=3\gamma_y=\frac{9a}{2}K_2-\frac{3a}{2}\left(\frac{1}{4}K_1+K_3\right),$$

$$\delta_x=-\delta_y=-\sqrt{3}\left(\frac{1}{2}K_1-K_3\right). \quad (\text{A6})$$

Using these relations we obtain from Eqs. (6) and (8) the optical-phonon frequency

$$\omega_o=\sqrt{\frac{3(K_1+K_3)}{M_C}}, \quad (\text{A7})$$

where  $M_C$  is the mass of the carbon atom, and the acoustic-phonon velocity

$$v_o=a\sqrt{\frac{3(4K_1K_2+3K_1K_3+4K_2K_3)}{16(K_1+K_3)M_C}}. \quad (\text{A8})$$

The dimensionless electron-lattice coupling  $\lambda_i$  is now obtained according to its definition Eq. (22) together with Eq. (24). The resulting expressions for the optical- ( $i=o$ ) and acoustic- ( $i=a$ ) phonon modes are given by, respectively, Eq. (61) and Eq. (62). The third condition to determine the three spring constants is obtained from the acoustic-phonon frequency at  $q=\pi/a$  where the acoustic branch deviates from its linear  $q$  dependence. It reads

$$\omega_a\left(\frac{\pi}{a}\right)=\left(\frac{2K_1+16K_2+K_3-\sqrt{4K_1^2+2K_1(4K_2-K_3)+(K_3-4K_2)^2}}{2M_C}\right)^{1/2}. \quad (\text{A9})$$

<sup>1</sup>R. E. Peierls, in *Quantum Theory of Solids* (Clarendon, Oxford, 1955).

<sup>2</sup>M. J. Rice and S. Strässler, *Solid State Commun.* **13**, 125 (1973).

<sup>3</sup>M. T. Figge, M. Mostovoy, and J. Knoester, *Phys. Rev. Lett.* **86**, 4572 (2001).

<sup>4</sup>R. Egger and A. O. Gogolin, *Phys. Rev. Lett.* **79**, 5082 (1997); *Eur. Phys. J. B* **3**, 281 (1998).

<sup>5</sup>C. Kane, L. Balents, and P. A. Fisher, *Phys. Rev. Lett.* **79**, 5086 (1997).

<sup>6</sup>L. Balents and M. P. A. Fisher, *Phys. Rev. B* **55**, R11 973 (1997).

<sup>7</sup>H.-H. Lin, *Phys. Rev. B* **58**, 4963 (1998).

<sup>8</sup>K. Tanaka, H. Ago, T. Yamabe, K. Okahara, and M. Okada, *Int. J. Quantum Chem.* **63**, 637 (1997).

<sup>9</sup>Y. Huang, M. Okada, K. Tanaka, and T. Yamabe, *Solid State Commun.* **97**, 303 (1996).

<sup>10</sup>K. Harigaya and M. Fujita, *Phys. Rev. B* **47**, 16 563 (1993).

<sup>11</sup>R. Saito, M. Fujita, G. Dresselhaus, and M. Dresselhaus, *Phys. Rev. B* **46**, 1804 (1992).

<sup>12</sup>J. W. Mintmire, B. I. Dunlap, and C. T. White, *Phys. Rev. Lett.* **68**, 631 (1992).

<sup>13</sup>C. L. Kane and E. J. Mele, *Phys. Rev. Lett.* **78**, 1932 (1997).

<sup>14</sup>For a review, see R. Saito, G. Dresselhaus, and M. S. Dresselhaus, *Physical Properties of Carbon Nanotubes* (Imperial College Press, London, 1998).

<sup>15</sup>For a review, see B. I. Yakobson and R. E. Smalley, *Am. Sci.* **85**, 324 (1997).

- <sup>16</sup>A. J. Heeger, S. Kivelson, J. R. Schrieffer, and W. P. Su, *Rev. Mod. Phys.* **60**(3), 781 (1988).
- <sup>17</sup>H. Takayama, Y. R. Lin-Liu, and K. Maki, *Phys. Rev. B* **21**, 2388 (1980).
- <sup>18</sup>C. L. Kane, E. J. Mele, R. S. Lee, J. E. Fischer, P. Petit, H. Dai, A. Thess, R. E. Smalley, A. R. M. Verschueren, S. J. Tans, and C. Dekker, *Europhys. Lett.* **41**, 683 (1998).
- <sup>19</sup>W. Clauss, D. J. Bergeron, and A. T. Johnson, *Phys. Rev. B* **58**, R4266 (1998).
- <sup>20</sup>M. T. Figge, Ph.D. thesis, University of Groningen, 2000.
- <sup>21</sup>E. M. Brody and H. Z. Cummings, *Phys. Rev. Lett.* **21**, 1263 (1968).
- <sup>22</sup>G. D. Mahan, *Many-Particle Physics* (Plenum Press, New York, 1981).
- <sup>23</sup>A. M. Rao, E. Richter, S. Bandow, B. Chase, P. C. Eklund, K. A. Williams, S. Fang, K. R. Subbaswamy, M. Menon, A. Thess, R. E. Smalley, G. Dresselhaus, and M. S. Dresselhaus, *Science* **275**, 187 (1997).
- <sup>24</sup>D. Sánchez-Portal, E. Artacho, J. M. Soler, A. Rubio, and P. Ordejón, *Phys. Rev. B* **59**, 12 678 (1999).
- <sup>25</sup>M. J. Rice, A. R. Bishop, and D. K. Campbell, *Phys. Rev. Lett.* **51**, 2136 (1983); M. J. Rice, S. R. Phillpot, A. R. Bishop, and D. K. Campbell, *Phys. Rev. B* **34**, 4139 (1986).
- <sup>26</sup>J. Liu, H. Dai, J. H. Hafner, D. T. Colbert, R. E. Smalley, S. J. Tans, and C. Dekker, *Nature (London)* **385**, 780 (1997).
- <sup>27</sup>R. Al-Jishi and G. Dresselhaus, *Phys. Rev. B* **26**, 4514 (1982); R. Al-Jishi, L. Venkataraman, M. S. Dresselhaus, and G. Dresselhaus, *Chem. Phys. Lett.* **209**, 77 (1990); T. Aizawa, R. Souda, S. Otani, Y. Ishizawa, and C. Oshima, *Phys. Rev. B* **42**, 11 469 (1990).
- <sup>28</sup>A. Komnik and R. Egger, in *Electronic Properties of New Materials – Science and Technology of Molecular Nanostructures*, edited by Hans Kuzmany, Jörg Fink, Michael Mehring, and Siegmur Roth, AIP Conf. Proc. No. **486** (AIP, New York, 1999); cond-mat/9906150 (unpublished).
- <sup>29</sup>M. Bockrath, D. H. Cobden, J. Lu, A. G. Rinzler, R. E. Smalley, L. Balents, and P. L. McEuen, *Nature (London)* **397**, 598 (1999).
- <sup>30</sup>L. F. Sun, S. S. Xie, W. Liu, W. Y. Zhou, Z. Q. Liu, D. S. Tang, G. Wang, and L. X. Qian, *Nature (London)* **403**, 384 (2000).
- <sup>31</sup>A. A. Farajian, K. Esfarjani, and Y. Kawazoe, *Phys. Rev. Lett.* **82**, 5084 (1999).